POLITECNICO DI MILANO

SCUOLA DI INGEGNERIA INDUSTRIALE E DELL'INFORMAZIONE

DIPARTIMENTO DI FISICA

Sub-10-fs extreme ultraviolet laser pulses for the investigation of ultrafast molecular dynamics

Supervisor:
Prof. Mauro Nisoli

Assistant supervisor:
Dr. Matteo Lucchini

Master degree thesis by:
Federico Zonca
Matr. **864533**

Academic Year 2016–2017

Non arrenderti mai, perché

quando pensi che sia tutto

finito, è il momento in cui

tutto ha inizio.

- Jim Morrison

Contents

Contents ii

List of Figures iv

Abstract xii

Sommario xiv

Introduction xvi

1 XUV Pulse Generation and Monochromator theory 1

1.1 Introduction 1

1.2 High-order Harmonic Generation 1

1.2.1 Three Step Model 2

1.2.2 Lewenstein Model 7

1.2.3 Phase Matching 15

1.3 Time-delay compensated monochromator 18

1.3.1 Bandwidth requirement 18

1.3.2 Grating monochromator 20

1.3.3 Off-Plane Mount 22

1.3.4 Time-delay compensated monochromator in the off-plane mount 24

2 XUV Pulse Characterization **28**

2.1 Introduction 28

2.2 Theory of characterization 29

2.2.1 FROG-CRAB Technique 30

2.2.2 Simulations 33

2.3 Experimental Setup 35

2.3.1 Pulse compression 36

2.3.2 High-order Harmonics Generation 44

2.3.3 Harmonic selection 45

2.3.4 Harmonic characterization 47

2.4 Ptychographic reconstruction 53

2.5 Measurement Results 56

3 Ultrafast molecular dynamics **59**

3.1 Introduction 59

3.2 Relaxation dynamics of ethylene cation 59

3.3 Measurement process 64

3.4 Experimental results 68

3.4.1 Harmonic 9 68

3.4.2 Harmonic 11 71

3.4.3 Harmonic 13 76

4 Conclusion and further development **83**

Bibliography **85**

List of Figures

1.1 Visual representation of the Three Step Model for high-order harmonic generation: in the first row it is described the temporal evolution of the electric field, while in the second row there are the corresponding steps of the model, the first is quantum tunneling, then the electron is accelerated from an electric field, the last is the electron's recombination with the parent ion (adapted from [1]). 3

1.2 Electron kinetic energy normalized on ponderomotive energy, just before recombination, versus ionization phase θ_i (phase that describes the blue curve, from 0° to 90°) and recombination phase θ_r (phase that describes the red curve, fro m 90° to 360°). At the top of the figure it is also shown the electric field phase (temporal evolution $t = \theta/\omega_0$) (adapted from [2]). 6

1.3 Example of HHG: harmonics field composed by orders 9-11-13-15-17 and fundamental frequency (adapted from [2]). 7

1.4 Real and imaginary component of the trajectories vs. the harmonic. In this figure it has been introduced $\theta = \omega_0 t$. The dashed line is representing the three-step model classical solution (adapted from [2]). 13

1.5 Diffraction grating that, given in input a with light, splits the pulse in all its harmonics (adapted from [3]). 20

1.6 Scheme of a blazed grating. 21

1.7 Schematic representation of the Off-Plane mount configuration (adapted from [4]). 23
1.8 Setup scheme of the time-delay compensated monochromator with all its optical components (adapted from [4]). 25

2.1 Scheme of sideband generation process 29
2.2 Spectrograms generated by HH25. In (a) the IR intensity was $I_{IR} = 10^{11}\ W/cm^2$, while in (b) $I_{IR} = 10^{12}\ W/cm^2$. This intensity difference becomes clear looking to the number of SBs generated, where in (a) IR is sufficient to generate just 2 sidebands, in (b) thanks to higher intensity 5 SBs are visible. The parameters used are: Argon as ionization gas, XUV and IR are assumed to be both transform limited, $\tau_{XUV} = 5\ fs$, $\tau_{IR} = 10\ fs$ (adapted from [5]) 33
2.3 Frequency chirp after the pulse is passed through two different kind of mediums. In particular the first medium has positive D_2 (called second order dispersion, $D_2 = L{\cdot}$GVD, where L is the length of the medium and GVD is the Group Velocity Dispersion), so the higher frequency will come later then lowers. In the second medium, with negative D_2, it occurs the opposite respect the first case (adapted from [6]). 34
2.4 Effect of the IR and XUV spectral chirp on the HH spectrogram: in (a) it is represented the spectrogram of HH25 for transform limit (TL) pulse, (b) and (c) show the chirp of IR ($D_2^{IR} = 40\ fs^2$) and XUV ($D_2^{XUV} = -20\ fs^2$) respectively, and in (d) both the pulses are chirped. The dashed blue and orange lines represent the evolution of the SB center as function of the pump-probe delay. The XUV pulse has a temporal duration of 5 fs, and the IR of 10 fs with an intensity $I_{IR} = 10^{11}\ W/cm^2$. The gas used for ionization was Argon. (adapted from [5]) 35

2.5 Scheme of the 4 steps necessary to the measurement process . . 36
2.6 Scheme of the setup before the hollow-core fiber 37
2.7 Stabilization scheme before the hollow-core fiber. 38
2.8 Scheme of the four-quadrant sensor: the beam impinges on the sensors, and each of them collects a certain intensity value, then, comparing each quadrant's detected intensity, it is possible to know the x and y coordinates of the beam respect the center . . 39
2.9 Block scheme of a PID controller 40
2.10 In the blue image it is shown the spectrum of the IR pulse before the hollow core fiber, while on the red is shown the spectral broaden related to the Self-Phase Modulation (SPM). 41
2.11 Schematic representation of a chirped mirror (adapted from [7]). 43
2.12 Scheme of our chirped mirrors setup. After the fiber the pulse is focused thanks a convergent mirror of radius $R = -3000\ mm$, then seven chirped mirrors introduce a negative dispersion that allow the pulse compression. After this stage the temporal duration of the IR beam is around 10 fs. After this stage the pulse is ready to be used to generate HHs. 44
2.13 Scheme of the generation chamber used in our setup 45
2.14 Scheme of the delay line: the piezoelectric is mounted over the carriage, and it moves the mirrors placed above, driven by the LabVIEW program 48
2.15 Scheme of the collinear overlapping setup. The XUV pulse is focused by the monochromator, so its spot size is smaller than the IR's. The XUV passes through the drilled mirror, while the IR is reflected. From now on the two beams proceed together: if the movable mirror is inserted they go on a beam profiler, else they enter in the time of flight (TOF) spectrometer. 49

2.16 LabVIEW program used, properly adopted for our scope. There are shown the required parameters that determine the scan duration, the scan saving settings and the spectrogram defined by the photogenerated electrons detected and the relative delay. 51

2.17 Representation of the generated harmonics. In particular, here are shown from left to right H13, H11 and H9. 53

2.18 Examples of FROG-CRAB reconstruction with PCGPA and LSGPA. The first column shows the simulated data, the second and the third respectively PCGPA and LSGPA methods used to reconstruct the data. For each column, from the top to the bottom are represent: the spectrogram, the temporal behavior of IR and XUV (HH25), the spectral amplitude (solid) and the phase (dashed). For the simulation the following characteristics have been used:$\tau_{XUV} = 7.5\ fs$, $\tau_{IR} = 15\ fs$, $D_2^{XUV} = -20\ fs^2$, $D_2^{IR} = -60\ fs^2$ and $I_{IR} = 10^{11}\ W/cm^2$ (adapted from [5]). . . . 54

2.19 Example of ePIE algorithm: the first two columns show the simulated and reconstructed spectrograms, while the third and the fourth display the simulated and reconstructed XUV and IR pulses. In the first row it has been considered a TL pulse, in the second a chirped XUV with $D_2^{XUV} = -20\ fs^2$, in the third both IR and XUV are chirped with $D_2^{XUV} = -20\ fs^2$ and $D_2^{IR} = -60\ fs^2$, in the last row the two pulses are still chirped as in row 3, but the IR intensity has been increased from $10^{11}\ W/cm^2$ to $10^{12}\ W/cm^2$. The time durations $\tau_{IR} = 15\ fs$ and $\tau_{XUV} = 7.5\ fs$ are the same for all the simulations. The sample temporal step used was of $2\ fs$, and reconstruction runs over 2000 iterations. (adapted from [5]) 56

2.20 Example of application of ePIE algorithm to experimental results. Two harmonics have been analyzed, the 27-th in the first row and the 19-th in the second row. In the first column are shown the experimental spectrograms, in the second the reconstructed, in the third are displayed the experimental and the reconstructed harmonic amplitude (respectively green and black dot) and phase(red and blue dot), in the fourth it is shown the pulse reconstruction in time (adapted from [5]). 57

3.1 (a) XUV spectrum of the HHs used in the experiment together with the first five states of molecular cation [8]. (b) Initial state population calculated with the partial cross-section taken from [9] and harmonic spectra in (a). 61

3.2 Potential Energy Surfaces (PES) for ethylene cation. In particular $\tilde{X}$ represent the ground state, while $\tilde{A}$, $\tilde{B}$ and $\tilde{C}$ represent the first three exited states (adapted from [10]). 62

3.3 (a) Schematic representation of the internal relaxation from an excited cation state to its ground state after XUV excitation. (b) After a certain delay (properly defined) the IR pulse can stop the relaxation process by giving the molecule sufficient energy to lose one of two H atoms (adapted from [11]). 63

3.4 Harmonic spectrum in an energetic scale. From left to right there are shown H9 ($\approx 14\ eV$), H11 ($\approx 17\ eV$) and H13 ($\approx 20\ eV$), and in dotted line the fragmentation threshold energy. 64

3.5 Schematic representation of a time of flight spectrometer (TOF). TOF can work both in electron and ion mode, in particular in the image ion mode is activated: the sample is injected inside the spectrometer thanks to a needle, then the laser pulse ionize the gas so that ions can be extracted, so that they are free to move along the drift tube and they can be detected by a MCP. 65

3.6 Graphics of the equations describing the decay and formations terms. 67

3.7 Ion mass spectrum from harmonic 9.The arrows mark $C_2H_2^+$, $C_2H_3^+$, $C_2H_4^+$. 69

3.8 $C_2H_2^+$ yield as function of the delay between the two pulses, in the case of H9. Experimental data and a proper fitting are shown with a value t_0 that represents the point at which the dynamics begins. 69

3.9 $C_2H_3^+$ yield as function of the delay between the two pulses, in the case of H9. Experimental data and a proper fitting are shown with a value t_0 that represents the point at which the dynamics begins. 70

3.10 $C_2H_4^+$ yield as function of the delay between the two pulses, in the case of H9. Experimental data and a proper fitting are shown with a value t_0 that represents the point at which the dynamics begins. 71

3.11 Ion mass spectrum from harmonic 11. In particular there are $C_2H_2^+$, $C_2H_3^+$, $C_2H_4^+$. This spectrum has been considered at the beginning of the scan, so others ions are not still visible. H_2O^+ comes from the background 72

3.12 $C_2H_2^+$ yield as function of the delay between the two pulses, in the case of H11. Experimental data and a proper fitting are shown with a value t_0 that represents the point at which the dynamics begins. 72
3.13 $C_2H_3^+$ yield as function of the delay between the two pulses, in the case of H11. Experimental data and a proper fitting are shown with a value t_0 that represents the point at which the dynamics begins. 73
3.14 $C_2H_4^+$ yield as function of the delay between the two pulses, in the case of H11. Experimental data and a proper fitting are shown with a value t_0 that represents the point at which the dynamics begins. 74
3.15 CH_2^+ yield as function of the delay between the two pulses, in the case of H11. Experimental data and a proper fitting are shown with a value t_0 that represents the point at which the dynamics begins. 75
3.16 H^+ yield as function of the delay between the two pulses, in the case of H11. Experimental data and a proper fitting are shown with a value t_0 that represents the point at which the dynamics begins. 76
3.17 Ion mass spectrum from harmonic 13. In particular there are, from left to right, H^+, CH_2^+, $C_2H_2^+$, $C_2H_3^+$, $C_2H_4^+$. OH^+ and H_2O^+ come from the background. 77
3.18 $C_2H_2^+$ yield as function of the delay between the two pulses, in the case of H13. Experimental data and a proper fitting are shown with a value t_0 that represents the point at which the dynamics begins. 77

3.19 $C_2H_3^+$ yield as function of the delay between the two pulses, in the case of H13. Experimental data and a proper fitting are shown with a value t_0 that represents the point at which the dynamics begins. 78
3.20 $C_2H_4^+$ yield as function of the delay between the two pulses, in the case of H13. Experimental data and a proper fitting are shown with a value t_0 that represents the point at which the dynamic begins. 79
3.21 C_2H^+ yield as function of the delay between the two pulses, in the case of H13. Experimental data and a proper fitting are shown with a value t_0 that represents the point at which the dynamics begins. 80
3.22 CH_2^+ yield as function of the delay between the two pulses, in the case of H13. Experimental data and a proper fitting are shown with a value t_0 that represents the point at which the dynamics begins. 81
3.23 H^+ yield as function of the delay between the two pulses, in the case of H13. Experimental data and a proper fitting are shown with a value t_0 that represents the point at which the dynamics begins. 82

Abstract

The aim of this thesis work is to investigate ultrafast molecular dynamics making use of sub-10-femtosecond ($1\ fs = 10^{-15}\ s$) laser pulses in the extreme ultraviolet regime (XUV or EUV). Indeed, many interesting molecular dynamics happen in few-femtosecond temporal scales and, in order to investigate them, it is necessary to generate and characterize shorter laser pulses. The main process that allows us to obtain such pulses is called high-order harmonic generation (HHG). In the HHG process a high intense short infrared (IR) pulse is focused on a gas target to produce the odd orders harmonics, that are multiples of the fundamental frequency of the IR. A comb of frequencies is therefore obtained, but in order to do selective pump-probe, only one harmonic must be taken. To select just one particular wavelength we used a time-delay compensated monochromator that is composed by two off-plane mount gratings placed in a subtractive configuration, so that temporal and spectral broadening introduced by the first monochromator are canceled by the second one. After harmonic selection, characterizing the pulse becomes of crucial importance to know the temporal resolution that we can exploit in our experiments. For the pulse characterization we applied the FROG-CRAB technique, starting from the experimental spectrogram obtained from the photoelectrons generated by the interaction of XUV pulse with a noble gas, changing the delay with the IR pulse. For the reconstruction it has been used an iterative algorithm called extended Ptychographic Iterative Engine (ePIE) properly adapted. Thanks to this approach we have been able to reconstruct

XUV pulses with $5 \pm 0.5\ fs$ of temporal duration that, at this moment, are the shortest ever measured. With such pulses we can study ultrafast molecules dynamics, including relaxation dynamics of the excited states of ethylene. We chose to analyze ethylene because it is, along with the isoelectronic neutral vinyl, the simplest organic π radical system, and at current moment it is not fully understood.

Sommario

Questo lavoro di tesi si pone come obiettivo l'investigare dinamiche molecolari ultraveloci per mezzo di impulsi laser di durata inferiore ai 10 femtosecondi ($1\ fs = 10^{-15}\ s$) nel regime degli estremi ultravioletti (EUV o anche XUV). Infatti, parecchie dinamiche molecolari avvengono su scale temporali di pochi femtosecondi, e affinché sia possbile studiarle in modo adeguato, risulta necessario generare e caratterizzare impulsi laser con durate temporali inferiori. Il principale processo che sfruttiamo per ottenere questo tipo di impulsi è la generazione di armoniche di ordine elevato, in inglese high-order harmonic generation (HHG). Il fenomeno di HHG avviene focalizzando un impulso infrarosso (IR) su una celletta contenente del gas, così da produrre le armoniche date da multipli dispari della frequenza fondamentale dell'IR. Si ottiene così un pettine di frequenze, ma per poter effettuare una misura di pump-probe selettivo, è necessario prenderne solo una. Per selezionare una singola armonica abbiamo utilizzato un monocromatore compensato in tempo, composto da due gratings posti in una configurazione sottrattiva, cosicché l'allargamento temporale e spettrale introdotti dal primo grating vengano annullati dal secondo. Dopo aver selezionato una singola armonica, la caratterizzazione delle proprietà temporali dell'impulso diventa di cruciale importanza perché ci consente di conoscere con quale risoluzione temporale possiamo condurre i nostri esperimenti. Per la caratterizzazione dell'impulso abbiamo applicato la tecnica FROG-CRAB, partendo dallo spettrogramma sperimentale ottenuto dai fotoelettroni generati dall'interazione tra l'impulso XUV e un gas

nobile, al variare del ritardo con l'impulso IR. Per la ricostruzione è stato applicato un algoritmo iterativo chiamato in inglese extended Ptychographic Iterative Engine (ePIE) adattato alle nostre necessità. Grazie a questo approccio siamo riusciti ad ricostruire impulsi della durata temporale di $5 \pm 0.5\ fs$, che sono al momento attuale i più corti mai misurati. Con questi impulsi siamo in grado di investigare dinamiche molecolari ultraveloci, tra cui quelle di rilassamento negli stati eccitati dell'etilene. Abbiamo scelto di studiare l'etilene in quanto, assieme al vinile, è il più semplice sistema organico con radicale π e finora le sue dinamiche non sono state ancora capite del tutto.

Introduction

A large number of dynamical processes in atoms and molecules evolves on timescales ranging from the femtosecond ($1\ fs = 10^{-15}\ s$) to the attosecond ($1\ as = 10^{-18}\ s$) domain. For this reason, their investigation requires the use of ultrashort light pulses. Ultrashort pulses with a sub-femtosecond duration, guarantee to observe in real-time the temporal evolution of many molecular dynamics by using proper experimental techniques. The most used approach to study ultrafast phenomena is called pump-probe: the first pulse (pump) excites the system under investigation, activating a particular phenomenon, than the second pulse (probe), properly synchronized with the first one, samples the evolution of the process. This measurement is repeated changing the delay between the two pulses, until the complete temporal evolution of the process is measured.

The temporal duration of a pulse is limited by its optical cycle. For example, considering a pulse in the infrared (IR) region with a wavelength λ of 800 nm, the optical cycle is $T = \lambda/c \simeq 2.67\ fs$ (where c is the speed of light in vacuum), so for such pulse it is impossible to reach a shorter temporal duration. To further reduce this value, ultraviolet (UV) and extreme ultraviolet (EUV or XUV) pulses must be used. In this way, even attoseconds can be generated. XUV pulses can be produced by using the process of High-order Harmonic Generation (HHG) in gases, which is a strongly non-linear process, allowing one to generate several harmonics of the fundamental frequency. HHG occurs when a strong IR beam

($I_{IR} \approx 10^{14}\ W/cm^2$) is focused on a gas target (usually a noble gas is used), so odd harmonics are produced from the input fundamental frequency. In a temporal domain picture, this process corresponds to the generation of a train of sub-femtosecond pulses.

In order to obtain a good spectral resolution, preserving a femtosecond temporal resolution, it is required to select a single harmonic: this selection process is achieved by using a Time-Delay Compensated Monochromator (TDCM) [4], that is composed by two off-plane mount gratings (two toroidal mirror and a blazed grating) in a subtractive configuration so that the temporal and spectral dispersion introduced by the first grating can be compensated for by the second one. The two gratings are separated by a slit that allows one to select only one specific harmonic. This monochromator has the advantages of preserving the temporal duration of the harmonic pulses. Thanks to this approach, single harmonics characterized by temporal duration of few-femtosecond have been obtained and used for pump-probe in gas phase.

Once the single harmonic has been selected, the characterization of the pulse is fundamental to understand the temporal resolution that has been achieved after the monochromator stage. Many techniques have been developed in the last decade to characterize the temporal properties of XUV ultrashort pulses for example the FROG-CRAB (*Frequency-Resolved Optical Gating for Complete Reconstruction of Attosecond Bursts*) technique [12]. The XUV pulse is focused on a gas target so that photoelectrons are generated, then the IR beam, properly synchronized with the XUV, modifies the energy of these electrons. This process, repeated for different delays, allows the construction of an energy spectrogram, from which it is possible to reconstruct the original XUV pulse. While this technique has been extensively tested and investigated for isolated attoseconds pulses, its extension to few-femtoseconds XUV is not trivial and has still to be proven, as a consequence of a reduction of information redundancy in the

FROG-CRAB spectrogram. In our case we were able to adapt a reconstruction algorithm that allowed us to measure XUV pulses with a duration down to 5 fs. These ultrashort pulses were used to investigate ultrafast molecular dynamics. In particular, we concentrated on the detection of relaxation dynamics occurring in ethylene cation ($C_2H_4^+$) that represents the simplest π radical. Even though this kind of dynamics have been object of interest for the last 30 years, nowadays they are still not completely understood [13]. The objective is the determination of the molecular paths followed by the molecule after excitation.
In detail, this thesis work is organized as follows:

- The **first chapter** is composed by two parts: the first one contains a theoretical description of the HHG process with the discussion of a semiclassical model called Three-Step Model (TSM), and of a quantum model introduced by Lewenstein *et al.* in 1994. Phase matching condition to achieve the maximum of generation from HHG are briefly treated. Then, in the second part I present the main elements that compose the time-delay compensated monochromator, and for each of them a short theoretical discussion.

- The **second chapter** presents all those elements that are necessary to fully characterize an XUV pulse. In particular, I present a theoretical discussion about the FROG-CRAB technique, the setup build with all its components, an overview on the reconstructing algorithm adopted and an analysis of the obtained results.

- The **third chapter** reports on the application of the ultrashort XUV pulses at the output of the monochromator. In detail, I will present a short theoretical description about ethylene dynamics that motivated our research, an overview on the components used to do the measurements and a discussion on the pump-probe measurement achieved considering different intensities of the probe (IR) pulses.

- The **fourth chapter** gives the conclusions of the work done and presents an overview on possible future applications and improvements for the present setup.

Chapter 1

XUV Pulse Generation and Monochromator theory

1.1 Introduction

In the first part of this chapter I will describe how extreme-ultraviolet light pulses (EUV or XUV) can be generated starting from an infrared (IR) strong field, presenting two different models, one semiclassical, the other based on quantum mechanics, then the phase matching conditions to get the maximum of generation intensity. In the second part I will present how the high-order harmonics are split and optimized thanks to a time-delay compensated monochromator, describing how it works.

1.2 High-order Harmonic Generation

It is possible to generate ultrashort XUV pulses exploiting a strongly nonlinear process called High-order Harmonic Generation (HHG). HHG is obtained from an intense laser pulse ($I \approx 10^{14}\ W/cm^2$) interacting with molecules or atoms, in particular noble gases are often used. Such interaction causes the emission of coherent light radiation at frequencies that are odd multiples of the IR pulse

frequency and with the same repetition rate. The choice of the molecules or atoms determine the order of the harmonics that will be generated and also their cut-off: intensity is indeed a crucial factor that defines both where the generation starts and where it stops due to saturation. This process allows us to obtain ultrashort XUV coherent pulses from an IR laser. HHG has been rather efficiently described first with a semiclassical approach called Tree Step Model, and then a quantum description has been fulfilled in 1994 by Lewenstein *et. al* [14].

1.2.1 Three Step Model

Even though HHG is a phenomenon that finds an exhaustive description only due to a pure quantum perturbation theory, many features can be intuitively and even quantitatively explained in terms of electron rescattering trajectories. In order to apply this semiclassical model it is important to consider the two following approximation:

- *Single Active Electron (SAE) approximation*: laser's electric field interacts just with one electron at a time.
- *Strong Field Approximation (SFA)*: in continuum, the effect of the atomic potential on the electron motion can be neglected, as it would be in a free particle regime.

This semiclassical approach is composed by the following steps:

1. *Tunneling ionization*: an electron is lifted to the continuum at the nuclear position with no kinetic energy through tunneling ionization; this process is achieved because of the input strong laser electric field, that bends the Coulomb atomic potential felt by the electron.
2. *Propagation*: the electron motion is governed classically by an oscillating electric field.

3. *Recombination*: half an optical cycle after the ionization moment, the electron feels a variation of verse of the field so, there is a non null probability that it could recombine with its nucleus with an acceleration that determines the emission of a photon. The emitted photon has a frequency that is proportional to the sum of the kinetic energy of the electron and the ionization potential I_p:

$$\hbar\omega = E_{kin} + I_p \tag{1.1}$$

In this model ionization and recombination are defined by quantum mechanics while propagation is completely classically treated.

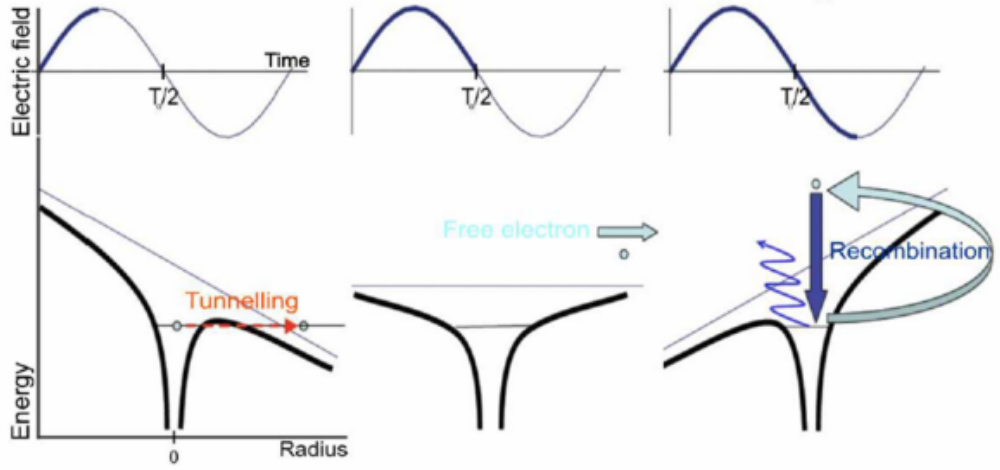

Figure 1.1: Visual representation of the Three Step Model for high-order harmonic generation: in the first row it is described the temporal evolution of the electric field, while in the second row there are the corresponding steps of the model, the first is quantum tunneling, then the electron is accelerated from an electric field, the last is the electron's recombination with the parent ion (adapted from [1]).

The first step of the model is described assuming the input pulse highly intense, so that it is possible to evaluate the ionization probability thanks to ADK theory (from the physicists Ammosov, Delone e Kraĭnov) [15]. The electron propagation can be studied just considering the contribution of the electric field because the magnetic field is so weak that it can be neglected. Let's assume an electric field $E(t)$ linearly polarized along z axis:

$$E(t) = E_0 \cos(\omega_0 t) \tag{1.2}$$

where E_0 is the field amplitude and ω_0 is its frequency. The fact that the polarization is linear is of fundamental importance, because it has been demonstrate that this is the kind of polarization that maximize HHG, while circular is the case that makes null generation. Considering $t = t_i$ the instant when the electron is ejected (ionization time), the equation of motion for the electron position $z(t)$ is given solving Newton equation written in atomic units:

$$\frac{d\dot{z}(t)}{dt} = E_0 \cos(\omega_0 t) \tag{1.3}$$

Choosing for simplicity the boundary conditions:

$$z(t_i) = 0 \tag{1.4}$$

$$\dot{z}(t_i) = 0 \tag{1.5}$$

one would get, for any $t > t_i$:

$$z(t) = -\frac{E_0}{\omega_0^2}[(\cos(\omega_0 t) - \cos(\omega_0 t_i)) + (\omega_0 t - \omega_0 t_i)\sin(\omega_0 t_i)] \tag{1.6}$$

$$\dot{z}(t) = \frac{E_0}{\omega_0}[\sin(\omega_0 t) - \sin(\omega_0 t_i)] \tag{1.7}$$

It is convenient to introduce the phase $\theta \equiv \omega_0 t$. Then the equation (1.6) can be written as:

$$z(\theta) = -\frac{E_0}{\omega_0^2}[\cos(\theta) - \cos(\theta_i) + (\theta - \theta_i)\sin(\theta_i)] \tag{1.8}$$

In this notation the kinetic energy of the electron becomes:

$$E_k(\theta) = \frac{1}{2}\dot{z}(\theta)^2 = 2U_p(\sin(\theta) - \sin(\theta_i))^2 \tag{1.9}$$

where $U_p = \frac{E_0^2}{4\omega_0^2}$ is the ponderomotive energy, that is the cycle-averaged quiver energy of a free electron in an electromagnetic field.

The recombination time (phase) t_r (θ_r) can be evaluated solving the motion equation in the case $z(t_r) = 0 \quad (z(\theta_r) = 0)$. So it is obtained:

$$\cos(\theta_r) - \cos(\theta_i) + (\theta_r - \theta_i)\sin(\theta_i) = 0 \tag{1.10}$$

The path that is done by the electron from θ_i to θ_r is call trajectory. It can be proved that the electron can recombine only if $0° < \theta_i < 90°$ otherwise if $90° < \theta_i < 180°$ it flies away and never recombines to the nucleus.

Looking for the maximum value for $E_{kin}(\theta)$ from equation (1.9), it is obtained the value of $3.17\,U_p$ when $\theta_i = 18°$ and $\theta_r = 252°$, so it is defined the cut-off frequency accordingly to equation (1.1):

$$\omega_{cutoff} = \frac{3.17\,U_p + I_p}{\hbar} \tag{1.11}$$

For fixed kinetic energies smaller or equal than $3.17\ U_p$ it is possible to find the trajectory solution of the coupled equations (1.9) and (1.10). As shown in figure (1.2), from the coupled equations are found two different trajectories:

- *long trajectory*: in the case of $0° < \theta_i < 18°$ and $252° < \theta_r < 360°$
- *short trajectory*: in the case of $18° < \theta_i < 90°$ and $90° < \theta_r < 252°$

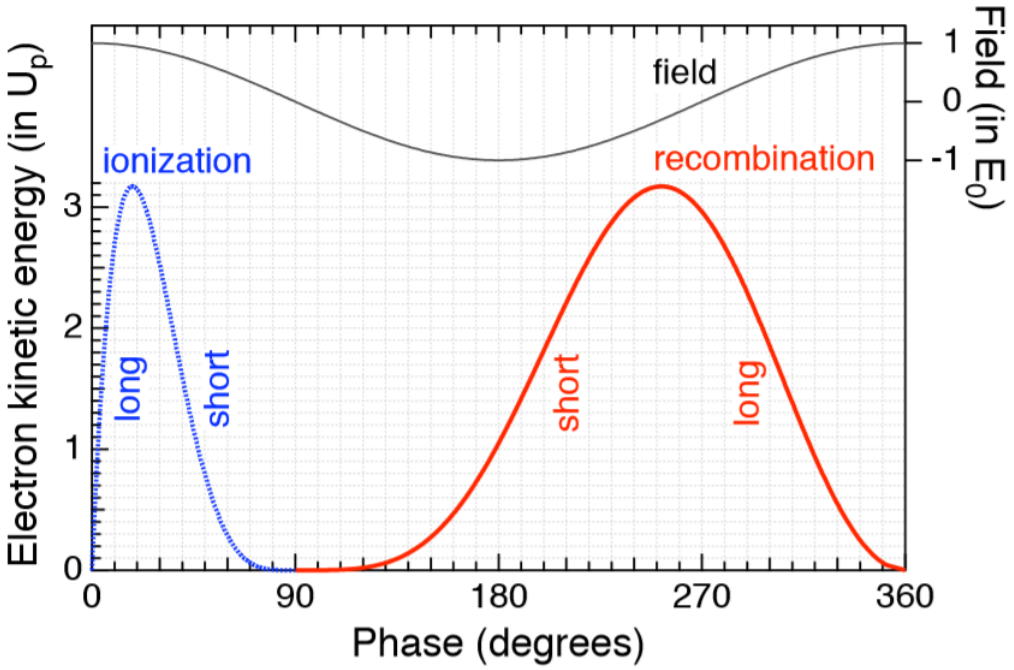

Figure 1.2: Electron kinetic energy normalized on ponderomotive energy, just before recombination, versus ionization phase θ_i (phase that describes the blue curve, from 0° to 90°) and recombination phase θ_r (phase that describes the red curve, fro m 90° to 360°). At the top of the figure it is also shown the electric field phase (temporal evolution $t = \theta/\omega_0$) (adapted from [2]).

Given a solution of the trajectory of the electron (θ_i,θ_r) from the above coupled equations, also the pair ($\theta_i + m\pi$, $\theta_r + m\pi$) is a solution, where m is an integer value, so the solution $z(\theta)$ can be rewritten as:

$$z_m(\theta) = (-1)^m z_{m=0}(\theta - m\pi) \tag{1.12}$$

where:

$$z_{m=0}(\theta) = \frac{E_0}{\omega_0^2}[\cos(\theta) - \cos(\theta_i) + (\theta - \theta_i)\sin(\theta_i)] \tag{1.13}$$

The equation (1.13) means that each half optical cycle harmonics are emitted with an alternating phase, such that the electric field can be expressed as:

$$E_h(t) = ... + F_h\left(t + \frac{2\pi}{\omega_0}\right) - F_h\left(t + \frac{\pi}{\omega_0}\right) + F_h(t) - F_h\left(t - \frac{\pi}{\omega_0}\right) + F_h\left(t - \frac{2\pi}{\omega_0}\right) + ... \tag{1.14}$$

Applying the Fourier transform to the above equation one would find the

frequencies of the emitted harmonics, with non null terms only for odd multiples of the fundamental ω_0. This explain why only the odd harmonics can be emitted. Because HHG is e phenomenon that is generated from the interaction of the electric field with many atoms, its efficiency is strictly correlated to *phase matching conditions* [16]: it is of fundamental importance in the choice of a particular trajectory that minimize the pulse duration of the XUV [17], but this concept will be better analyzed in following parts.

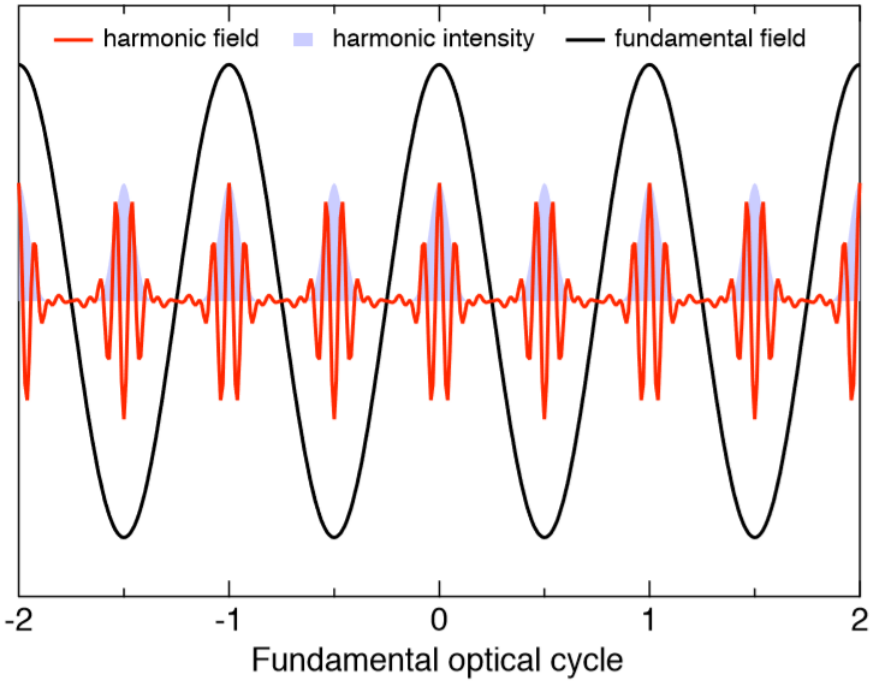

Figure 1.3: Example of HHG: harmonics field composed by orders 9-11-13-15-17 and fundamental frequency (adapted from [2]).

1.2.2 Lewenstein Model

The above description of HHG phenomenon was composed by a classical part (electron propagation) and two quantum mechanics section (Tunneling and Recombination), but it neglects some important phenomena like the quantum diffusion of the wave packets, the elastic scattering from the parent ion and the quantum interference between wave packet generated in different temporal instants. The aim of Lewenstein *et al.*[14] was to go over the classical description

limitations and obtain a quantum dissertation for High-order Harmonic Generation. The interaction of an atom with a laser pulse, which field $\mathbf{E}(t)$ is linearly polarized along z direction, is described by the time dependent Schrödinger equation (TDSE) in length gauge:

$$i\frac{\partial\Psi(\mathbf{r},t)}{\partial t} = \left[-\frac{1}{2}\nabla^2 + V(\mathbf{r}) + z\mathbf{E}(t)\right]\Psi(\mathbf{r},t) \tag{1.15}$$

where $V(\mathbf{r})$ is the atomic potential. Initially the state is in the ground state denoted as $|0\rangle$ which has, in general, spherical symmetry. In the assumption of weak ionization, so that U_p should be large but still below the saturation level U_{sat}, all atoms ionize during interaction time. In this condition tunneling becomes valid. In order to achieve analytical results, first of all it has been necessary to introduce the following approximations:

(a) *Single Active Electron (SAE) approximation*: The contribution of all the excited bound states can be neglected except the ground state $|0\rangle$.

(b) *Small Perturbation approximation*: The depletion of the ground state can be neglected, $U_p < U_{sat}$.

(c) *Strong Field Approximation (SFA)*: In continuum, the effect of the atomic potential $V(\mathbf{r})$ on the electron motion can be neglected, as it would in a free particle regime.

Assumption (b) can be used only in case of intensities smaller than saturation intensity, otherwise the depletion of ground state must be considered. Assumptions (a) and (c) holds when there are no intermediates resonances and if Keldysh parameter $\gamma = \sqrt{I_p/2U_p}$ is smaller than one: this condition implies that when an electron appears in continuum it is under the influence of a strong field and when it comes back to its nucleus it has a large kinetic energy such that atomic

potential force can be neglected. In this case the generated harmonic will have higher energies, due to high energetic electrons, of the order $E_{2M+1} > I_p$.

There are different ways to solve equation 1.15, and one of them consists in considering one part of the interaction Hamiltonian as just a perturbation [18]. After (a) and (c) assumptions, the time-dependent wavefunction can be written as:

$$|\Psi(t)\rangle = |\Psi(t)\rangle_{bound} + |\Psi(t)\rangle_{free} \tag{1.16}$$

Where the bound component is:

$$|\Psi(t)\rangle_{bound} = e^{iI_p t} a(t) \, |0\rangle \tag{1.17}$$

with $a(t) \simeq 1$ is the ground state amplitude, while the free component can be written as:

$$|\Psi(t)\rangle_{free} = e^{iI_p t} a(t) \int d^3\mathbf{v} \, b(\mathbf{v}, t) \, |v\rangle \tag{1.18}$$

with $b(\mathbf{v}, t)$ that represent the amplitudes of the corresponding continuum state. This term can be calculated from the Schrödinger equation and results to be:

$$b(\mathbf{v}, t) = i \int_0^t dt' a(t') \mathbf{E}(t') \cdot \mathbf{d}[\mathbf{v} - \mathbf{A}(t) + \mathbf{A}(t')] \times e^{-iS(\mathbf{v},t,t')} \tag{1.19}$$

where:

- $\mathbf{d}(\mathbf{v}) = \langle \mathbf{v} | \, \mathbf{r} \, | 0 \rangle$ denotes the atomic dipole matrix element for bound-free transition, and d_z is the component parallel to polarization direction.
- $a(t)$ can be considered 1 in order to neglect ground state depletion.
- $\mathbf{A}(t) = -\int dt \mathbf{E}(t) = [0, 0, -E_0 \sin(w_0 t)]$ is the vector potential of the laser field.

- $S(\mathbf{v}, \mathbf{A}, t, t') = \int_{t'}^{t} dt''[(\mathbf{v} - \mathbf{A}(t) + \mathbf{A}(t')^2)/2 + I_p]$ is the *quasi-classical action*.

So the time-dependent wavefunction can be written in a compact form considering equations (1.16), (1.17), (1.18):

$$|\Psi(t)\rangle = e^{iI_p t}(a(t)\,|0\rangle + \int d^3\mathbf{v}\, b(\mathbf{v}, t)\,|\mathbf{v}\rangle) \tag{1.20}$$

Now given the equation (1.20) it is possible to calculate the z component of the time-dependent dipole moment:

$$z(t) = \langle\Psi(t)|\, z\,|\Psi(t)\rangle = \int d^3\mathbf{v}\, d_z{}^*(\mathbf{v}) b(\mathbf{v}, t) + c.c. \tag{1.21}$$

Writing the above formula has been neglected the Continuum-Continuum contribution [19] and has been considered just the transitions to the ground state.

It is now useful to introduce the canonical momentum as:

$$\mathbf{p} = \mathbf{v} + \mathbf{A}(t) \tag{1.22}$$

Applying this definition to equation (1.21) the dipole moment becomes:

$$z(t) = i \int_0^t dt' \int d^3\mathbf{p}\, \mathbf{E}(t') \cdot \mathbf{d}(\mathbf{p} - \mathbf{A}(t')) \cdot \mathbf{d}^*(\mathbf{p} - \mathbf{A}(t)) e^{-iS(\mathbf{p}, t, t')} + c.c. \tag{1.23}$$

This equation can be physically interpreted [20] in relation to the semiclassical Three Step Model:

- $\mathbf{E}(t') \cdot \mathbf{d}(\mathbf{p} - \mathbf{A}(t'))$ is the probability amplitude for an electron to make transition to the continuum at time t' with canonical momentum $\mathbf{p}$; this term is related to ionization at t'.

- $e^{-iS(\mathbf{p}, t, t')}$ represent the phase factor assumed by the electronic wavefunction until the time t. The effects of the atomic potential are assumed to be

small between t' and t so that $S(\mathbf{p}, t, t')$ can be considered as the classical description of the motion of a free electron in a laser field with a constant momentum $\mathbf{p}$.

- $\mathbf{d}^*(\mathbf{p} - \mathbf{A}(t))$ is the amplitude of recombination time of the electron with its nucleus.

It is interesting to notice that equation (1.23) allows also other two physical interpretation: In the first, the electron appears in continuum at time t with the kinetic momentum $\mathbf{p} - \mathbf{A}(t)$, then is propagated back until t' when it recombines to the ground state $|0\rangle$ with amplitude $\mathbf{E}(t') \cdot \mathbf{d}(\mathbf{p} - \mathbf{A}(t'))$. In the other way to look the above equation, it is possible to consider it as a Landau-Dyhne formula for transitions probabilities applied to the evaluation of the observable z [20]. In relation to the equation (1.23), the quasi-classical action changes very fast in respect to all the other terms, so it can be considered that, for $t - t'$ of the order of one period of the laser field, the main contribute to the integral over $\mathbf{p}$ is given by the stationary points of the quasi-classical action:

$$\nabla_{\mathbf{p}} S(\mathbf{p}, t, t') = 0 \tag{1.24}$$

On the other hand, $\nabla_{\mathbf{p}} S(\mathbf{p}, t, t') = 0$ can be expressed as the difference of position in space between the electrons evaluated in t and t':

$$\nabla_{\mathbf{p}} S(\mathbf{p}, t, t') = \mathbf{r}(t) - \mathbf{r}(t') \tag{1.25}$$

This means that the stationary points of the classical action correspond to those momenta for which the electron born in t' and returns to the same position at t. In other words, the dominant contribution to harmonic generation is given by those electrons which tunnel away from the nucleus, but then re-encounter it while oscillating in the laser field. So, the integral over $\mathbf{p}$ of equation (1.23)

might be solved thanks to the saddle-point method:

$$z(t) = i\int_0^{+\infty} d\tau \left(\frac{\pi}{\varepsilon + i\tau/2}\right)^{3/2} \mathbf{d}^*(\mathbf{p}_{st}(t,\tau) - \mathbf{A}(t))\cdot \\ \mathbf{d}(\mathbf{p}_{st}(t,\tau) - \mathbf{A}(t)) \cdot \mathbf{E}(t-\tau) e^{-iS_s t(t,\tau)} + c.c \tag{1.26}$$

where τ is called return time and is defined as the temporal duration of the electron path $t - t'$, the term $\left(\frac{\pi}{\varepsilon + i\tau/2}\right)^{3/2}$ has a positive infinitesimal ε, that is from the regularized Gaussian integration (it is introduced in order to eliminate the singularity for $\tau = 0$), takes into account of the quantum diffusion (in particular the spread of the electronic wave packet deposited to the continuum) and reduces the contribution of those trajectories with a long return time (τ much larger than a laser optical cycle). The cross-section of recombination is reduced when the value of return times becomes large.

It is now possible to determine the harmonic generation rate, considering modulus square of the Fourier Transform of the dipole moment:

$$W(\omega) \propto \omega^3 \left|z(\omega)\right|^2 \tag{1.27}$$

where:

$$z(\omega) = \int_{-\infty}^{+\infty} dt\, z(t) e^{-i\omega t} \tag{1.28}$$

in particular this last equation is a three dimensional integral, that can be solved again thanks to saddle-point method, but considering the Legendre transform on the quasi-classical action:

$$\Theta(\mathbf{p}_{st}, t, \tau) := \omega t - S(\mathbf{p}_{st}, t, \tau) \tag{1.29}$$

Using this function, one could write the new saddle-point equations:

$$\left.\frac{\partial \Theta}{\partial t}\right|_{t_{st}} = \omega - \frac{[\mathbf{p}_{st} - \mathbf{A}(t_{st})]^2}{2} - I_p = 0 \tag{1.30}$$

$$\left.\frac{\partial \Theta}{\partial t'}\right|_{t_{st}} = \frac{[\mathbf{p}_{st} - \mathbf{A}(t_{st})]^2}{2} + I_p = 0 \tag{1.31}$$

This two equations express the energy conservation at the ionization and recombination time. Due to the fact that the ionization potential can't be null, the solutions $(\mathbf{p}_{st}, t_{st}, \tau_{st})$ to equations (1.30), (1.31) are complex values, so also the associated trajectories are complex.

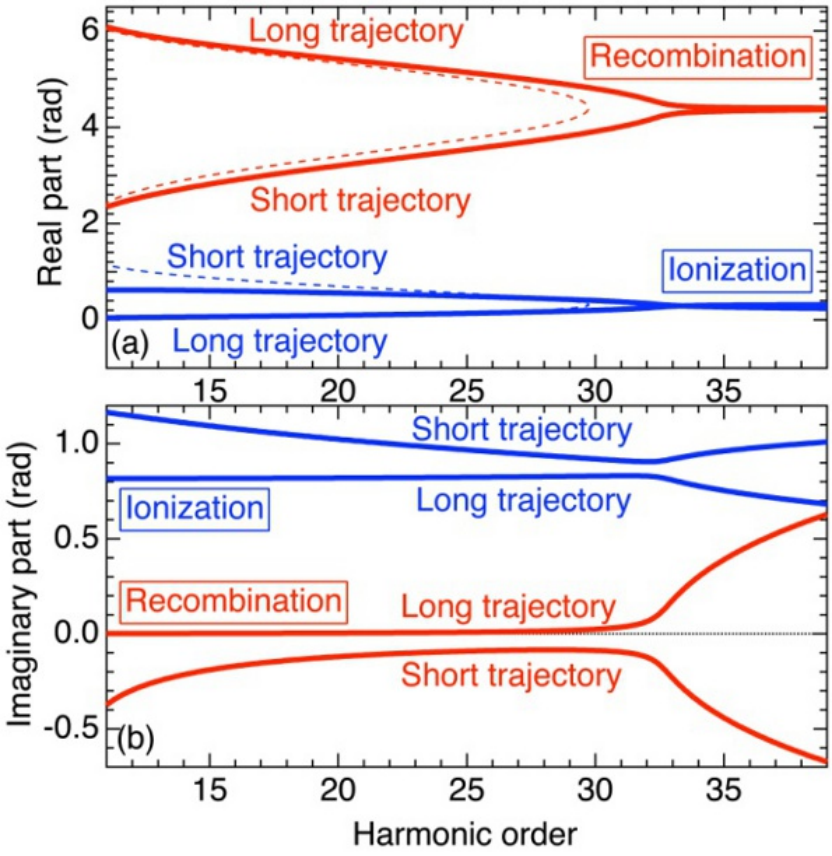

Figure 1.4: Real and imaginary component of the trajectories vs. the harmonic. In this figure it has been introduced $\theta = \omega_0 t$. The dashed line is representing the three-step model classical solution (adapted from [2]).

The Fourier transform of the dipole moment $z(\omega)$ can be approximated with a coherent superposition of these quantum path:

$$
\begin{aligned}
z(\omega) &= \sum_{st} |z(\omega)|\, e^{i\Phi_{st}(\omega)} \\
&= \sum_{st} \frac{i2\pi}{\sqrt{det(S'')}} \left(\frac{\pi}{\varepsilon + i\tau_{st}/2}\right)^{3/2} \mathbf{d}^*(\mathbf{p}_{st} - \mathbf{A}(t_{st}))\cdot \\
&\quad \mathbf{E}(t_{st} - t) \cdot \mathbf{d}(\mathbf{p}_{st} - \mathbf{A}(t_{st} - \tau_{st}))e^{-i[S(\mathbf{p}_{st}, t_{st}, \tau_{st}) + \omega t_{st}]}
\end{aligned} \tag{1.32}
$$

where $\Phi_{st}(\omega)$ is the phase of the complex dipole moment and $det(S'')$ is the determinant of the 2×2 matrix containing the second order derivatives of the function $\Theta(\mathbf{p}_{st}, t, \tau)$ with respect to t and t' in correspondence to the saddle-point solutions.

$$
S'' = \begin{bmatrix} \frac{\partial^2\Theta}{\partial t^2} & \frac{\partial^2\Theta}{\partial t \partial t'} \\ \frac{\partial^2\Theta}{\partial t' \partial t} & \frac{\partial^2\Theta}{\partial t'^2} \end{bmatrix} \tag{1.33}
$$

$$
\frac{\partial^2\Theta}{\partial t \partial t'} = \frac{(\mathbf{p} + \mathbf{A}(t))(\mathbf{p} + \mathbf{A}(t'))}{t - t'} \tag{1.34}
$$

$$
\frac{\partial^2\Theta}{\partial t^2} = -\frac{2(\omega - I_p)}{t - t'} - \mathbf{E}(t) \cdot (\mathbf{p} + \mathbf{A}(t)) \tag{1.35}
$$

$$
\frac{\partial^2\Theta}{\partial t'^2} = \frac{2I_p}{t - t'} + \mathbf{E}(t') \cdot (\mathbf{p} + \mathbf{A}(t')) \tag{1.36}
$$

Saddle-point solution $(\mathbf{p}_{st}, t_{st}, \tau_{st})$ that differ by the temporal duration of the electron path in continuum, can be derived considering each photon energy.

If one would consider only those trajectories which are characterized by the $Re(\tau) < T_0$, where T_0 is the period of the input laser field, he would be able to recognize two different kind of trajectories:

- *long trajectory*: the return time is around one optical cycle of the electric field of the laser.
- *short trajectory*: the return time is shorter than the half of the optical cycle of the electric field of the laser.

In this condition ($Re(\tau) < T_0$), the equation (1.32) can be approximated as the coherent superposition of just the 2 kind of trajectories described above, so only long and short quantum path:

$$z(\omega) \approx \sum_{short} |z_s(\omega)| \, e^{i\Phi_s(\omega)} + \sum_{long} |z_s(\omega)| \, e^{i\Phi_s(\omega)} \tag{1.37}$$

In this approximation it is interesting to see that the phase of the dipole moment induced on an atom by a driving laser pulse depends on the laser intensity and that the harmonic phase follows this intrinsic atomic phase [21] [16]. Because long and short trajectories have different ionizing and recombination time (so different quantum paths), different electrons are subjected to different electric fields, and so also their harmonic phases behave will be different. If the contribution of the two quantum path are added together in order to generate high order emission, different harmonics would randomly get distributed harmonic phase values. Lewenstein model predicts a cutoff energy:

$$E_{cutoff} = 3.17U_p + gI_p \tag{1.38}$$

where $g \approx 1.3$, making this prediction slightly higher than the one given by the three-step model. This is related to the fact that there is a finite distance between the nucleus and tunnel exit; the electron which has returned to the position of is further accelerated till it reaches the nuclear position.

1.2.3 Phase Matching

The maximum of efficiency in high-order harmonic generation is achieved when phase matching conditions are respected [22]. Let's consider the *q-th* harmonic, so its wavevector is $\mathbf{k}_q$: the optimal condition to generate harmonics is obtained in direction $\mathbf{k}_q$ if the harmonic fields generated in two different point

in the space, $\mathbf{r}_1$ and $\mathbf{r}_2$, make constructive interference:

$$arg[P_q(\mathbf{r}_1)e^{i\mathbf{k}_q(\mathbf{r}_2-\mathbf{r}_1)}] = arg[P_q(\mathbf{r}_2)] \tag{1.39}$$

where the arg function is a function that operates on complex values and returns the angle between the positive real axis and the complex vector and P_q stands for the *q-th* Fourier component of the atomic polarization in the medium. It is proportional to the atomic density and to the corresponding Fourier component of the atomic dipole moment. If $\mathbf{r}_1$ and $\mathbf{r}_2$ are close enough, the result of equation (1.39) is:

$$\mathbf{k}_q = \nabla arg(P_q) \tag{1.40}$$

In a perturbative regime, the modulus of the wave vector of the polarization of the *q-th* harmonic is just q times the incident-plane wave: $k_q = qk_0$, where $k_0 = \omega/c$.

Considering x the propagation axis ($x = 0$ represent the position of the focus) and r the distance from this axis (cylindrical coordinates), two other phase factor are involved:

- Intrinsic atomic phase term that depends on the intensity of the driving field:

$$\Phi_{at}(r, x) = q\omega t_{st} - S(\mathbf{p}_{st}, t_{st}, t'_{st}) \tag{1.41}$$

  where the semiclassical action S can be roughly approximated by $S \simeq -\tau_{st}U_p$ for those electrons with quantum path temporal duration τ_{st}.

- Phase induced by the focusing of the fundamental beam (*Gouy phase*); approximating the beam with a Gaussian shape, the phase becomes:

$$\Phi_{foc}(r, x) = arg\left[\frac{1}{b + 2ix}\exp\left(-\frac{k_0 r^2}{b + 2ix}\right)\right] \tag{1.42}$$

where b is the confocal parameter.

The total wavevector $\mathbf{k}_1$ of the fundamental Gaussian beam is space dependent:

$$\mathbf{k}_1(r,x) = k_0\mathbf{e}_x + \nabla\Phi_{foc}(r,x) \tag{1.43}$$

The effective wavevector $\mathbf{K}$ is dependent on the atomic phase term:

$$\mathbf{K}(r,x) = \nabla\Phi_{at}(r,x) \tag{1.44}$$

Therefore, the phase matching condition can be written as:

$$\mathbf{k}_q = q\mathbf{k}_1 + \mathbf{K} \tag{1.45}$$

It can be proved that this condition can be achieved in two different cases:

1. Generation on axis ($r = 0$) and after the focal point ($x > 0$): in this condition a *collinear* phase matching is achieved, so harmonics are efficiently generated along the propagation direction of the laser, also, the emitted harmonics get a Gaussian structure from the input field.

2. Generation off axis ($r > 0$) and before the focal point($x < 0$): in this condition a *non-collinear* phase matching is achieved, so the harmonics are not generated along propagation direction, and they have an annular structure.

These considerations show the importance of the propagation effects on the features of the emitted harmonic field. Since the atomic phase term depends on the time duration of the quantum path, the phase matching condition allow to favor or cancel one kind of trajectory or the other; in other words, it is possible to generate harmonics with just one particular kind of trajectory (long or short) changing geometrical focusing configurations. For example, in the case of a

Gaussian fundamental beam and an atomic medium placed after the focal point (case 1) all long trajectories contribution can be eliminated. In this case the resulting pulses are affected by an intrinsic positive *chirp* [23], given by the fact that low energy photons are emitted before those with higher energies.

1.3 Time-delay compensated monochromator

The process of high-order harmonic generation described in the previous section is of fundamental importance in all those experiments that require the study of ultrafast phenomena (every phenomenon which has temporal duration of the order of femtosecond or shorter). When harmonics are generated with the first kind of phase matching, they are all collinear, so the issue of selecting just few (or in case only one) of them is crucial in order to reduce the bandwidth such that it is possible to make selective probe. This selection implies, due to time-energy indetermination principles, a loss in temporal resolution, indeed attosecond pulses cannot be obtained anymore. In any case it is an acceptable price to pay if the dynamics that one wants to study are in the femtosecond region, as it is in our case. For this reason it becomes necessary to develop a monochromator that is able to select one harmonic. An important condition that must hold is that this process of selection must not influence the spatial and temporal characteristics of the pulse. This is a crucial element in order to obtain both high temporal resolution and high peak power [4].

1.3.1 Bandwidth requirement

The design of this kind of monochromator must include the analysis of the XUV pulse transformation in both the spectrum and the spectral phase. Therefore, the monochromator can be modeled as a filter with a complex frequency response $K(\omega)$. In the case of a Gaussian pulse with no modulation the product

of the spectral width at half-maximum times the temporal duration at half-maximum has a lower limit given by:

$$\Delta\omega_{1/2}\Delta\tau_{1/2} = 4\ln 2 = 2.77 \tag{1.46}$$

In order to maintain unchanged the temporal duration of the pulse as in equation (1.46), two conditions must be respected:

1. The bandpass transmitted by the monochromator $\Delta\omega_m$ has to be greater than the full width at half maximum of the input pulse $\Delta\omega_{1/2}$

2. The complex transfer function $K(\omega)$ must be approximatively constant in proximity of the harmonics frequencies.

While the first condition is simply verified because the harmonics peaks are well split, so it easily possible to set the monochromator in order to select one (or more) harmonic without introducing any modification in Fourier spectrum, the second condition is more difficult to achieve. Anyway, it can be demonstrated that it holds always if the monochromator is build using only reflecting optic elements, because variation of reflectivity of the coatings are really small so that can be considered as negligible: in this condition $K(\omega)$ is almost constant. Many techniques have been implemented in order to realize this kind of monochromator, but the most common is certainly based on dielectric multilayer mirrors in normal incidence: the success of this solution is related to its efficiency and to the fact that it does not modify the pulse duration more than a fraction of femtosecond. This approach is however limited by the lacking of tunability in the frequency domain (if one would like to study a different spectral region, he has to change the complete monochromator) and also by the fact that there not exists dielectric mirror for all the spectral region, so studying different harmonics with this setup is almost impossible. For these reasons it is useful to introduce a more flexible solution, based on the use of diffraction gratings.

1.3.2 Grating monochromator

The limits related to a dielectric multilayer monochromator have been discussed in the above sector, where has been highlighted a lack of tunability. This limit can be overcame thanks an ordinary diffraction gratings. A grating is an optical component that alters the optical path for the different wavelength that compose the pulse, so the result is a separation of all the frequencies.

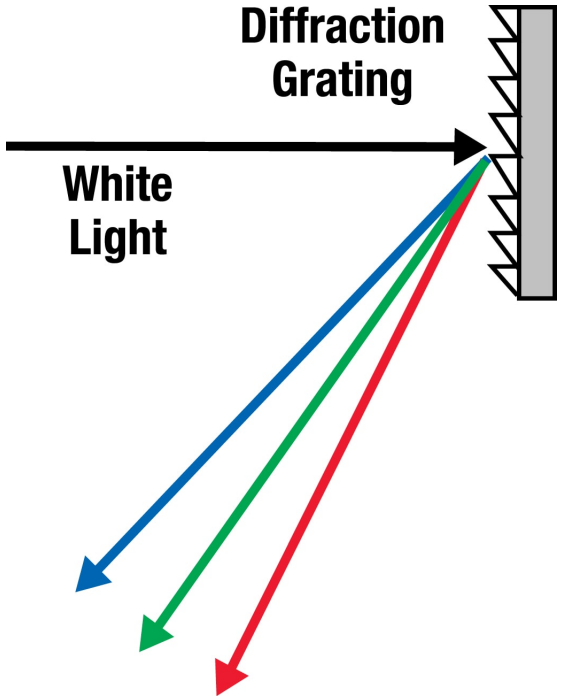

Figure 1.5: Diffraction grating that, given in input a with light, splits the pulse in all its harmonics (adapted from [3]).

The issue of this process is that the diffraction introduced by a grating gives a time broadening of the ultrafast pulse, indeed the total difference in the optical paths of the rays diffracted by N grooves illuminated by radiation at wavelength λ is $Nm\lambda$ where m is the order of diffraction. This effect can't be neglected in case of an input pulse of some femtosecond, so another approach is necessary: in order to avoid this issue, it can be used another gratings in a subtractive configuration and to compensate the dispersion. First of all, let's analyze each component of the grating monochromator, then how do they work in a double

grating configuration.

Blazed gratings

The blazed grating is one of the most common optical elements that are used in experiment where the selection of a singular frequency is a crucial factor. It is a particular kind of diffraction grating optimized to achieve the maximum efficiency in a given diffraction order, for this reason the maximum optical intensity is concentrated in one particular order, while the others are less efficient, for example, zeroth order act just a mirror and no frequency selection occur. It is composed by a constant line spacing determining the magnitude of the wavelength splitting. The grating line is characterized by a triangular sawtooth-shaped cross section that describes a step structure. The angle generated between a groove's longer side and the plane of the grating is called *blaze angle*.

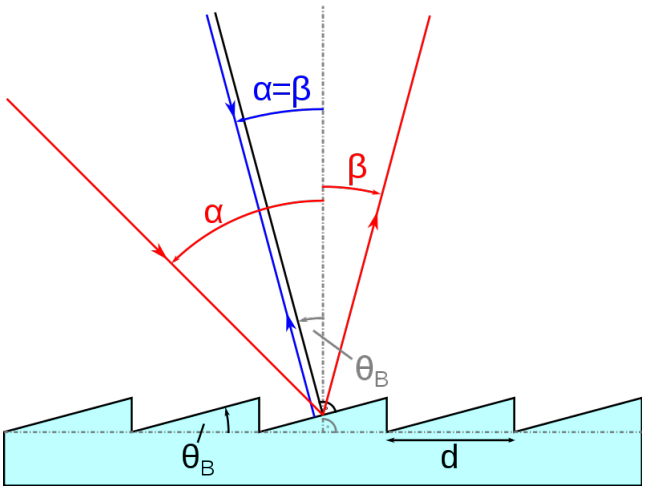

Figure 1.6: Scheme of a blazed grating.

The angles that guarantee the peaks of intensity are given by the following formula:

$$d(\sin\alpha + \sin\beta) = m\lambda \tag{1.47}$$

where:

- d is the constant distance between the two successive grooves.
- α is the angle at which the incident radiation arrives with respect to the normal of the grating.
- β is the angle respect to the normal of the diffracted radiation.
- m is the order of the peak and its values are both positive and negative integer numbers.
- λ is the wavelength of the incident radiation.

Toroidal mirror

Toroidal mirrors are optical elements characterized by different curvature radii along the two dimensions. The shape is an elliptic paraboloid with different in order to allow different focal distances depending on the angle of incidence of the radiation. This mirrors are covered by a metallic surface and are used with grazing incidence. The main advantage of using this kind of mirror is that they allows to achieve higher efficiency also in the XUV spectral region, where conventional coating have lower reflectivity.

1.3.3 Off-Plane Mount

The off-plane mount, also known as conical diffraction mount, is a one grating configuration monochromator and differs from the other kind of configuration because the incident and diffracted wave-vectors are almost parallel to the grooves [24].

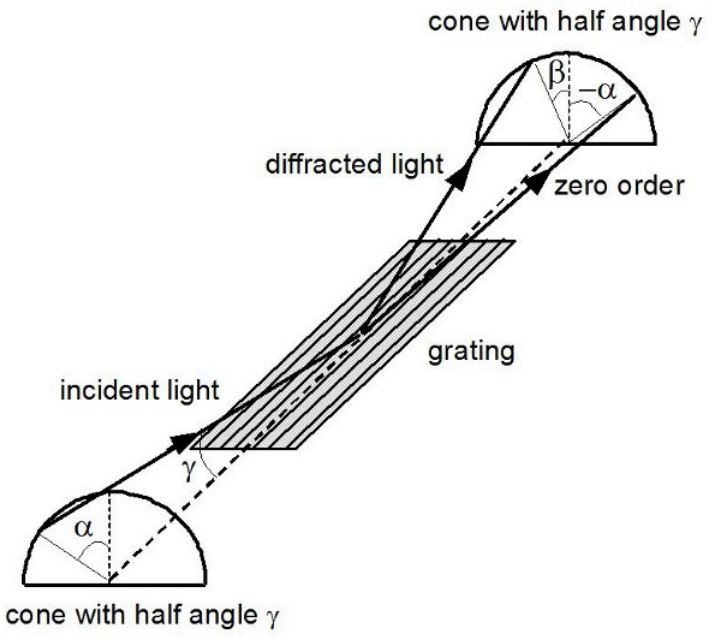

Figure 1.7: Schematic representation of the Off-Plane mount configuration (adapted from [4]).

In this scheme two parameters are necessary in order to describe the direction of the incoming rays:

- The angle γ between the direction of the incoming rays and the direction of the gratings and it describes the half-angle of the cone into which the light is diffracted.
- The azimuth α of the incoming rays is defined to be null if they lie in the plane perpendicular to the grating surface and parallel to the rulings.

Given this two parameters it is possible to define the azimuth of zeroth order as $-\alpha$, the azimuth of a generic diffracted order β and so the grating equation:

$$\sin\gamma(\sin\alpha + \sin\beta) = m\lambda\sigma \tag{1.48}$$

where m is the order of the gratings, λ is the wavelength of the incoming radiation and σ is the groove density. As seen in the above section this configuration is composed by a blazing gratings, such that the harmonics could be split in vertical

direction. The selection of just one harmonic takes place thanks a horizontal slit after the grating that is able to rotate around the tangential axis respect the surface. The maximum of efficiency is obtained when the light leaves the grating performing a specular reflection on the groove surface; this assumption can be expressed by the equation:

$$\alpha + \beta = 2\delta \tag{1.49}$$

where δ is the blaze angle and is an intrinsic property of the grating. In particular, the highest efficiency is obtained when $\alpha = \beta = \delta$, in other words, when the groove of the grating is seen by the incident radiation as a portion of a plane mirror. In this particular condition the equation (1.48) can be re-written as:

$$2 \sin \gamma \sin \delta = m\lambda\sigma \tag{1.50}$$

Since this condition has been achieved thanks the grating's rotation of a particular angle, the blaze optimization is given just for only one harmonic, while the other harmonics will be subject to a lack of efficiency. As discussed previously, a configuration with only one grating introduces a difference in the total optical path, so it is necessary to consider a two gratings scheme.

1.3.4 Time-delay compensated monochromator in the off-plane mount

This kind of monochromator is able to overcome the issues given by the use of a single monochromator, so makes possible the time-delay compensation. It work's principle is very simple: two off-plane mount are used in subtractive configuration, such that the delay introduced by the first is annihilated by the second. Therefore, such a monochromator requires six optical elements as shown in figure (1.8)

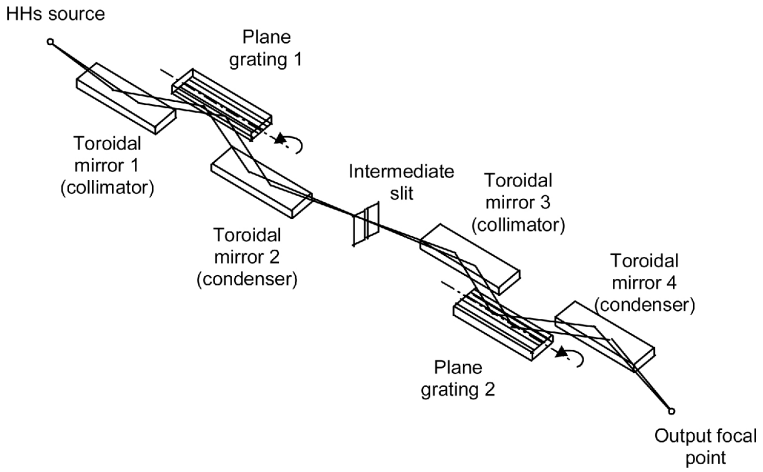

Figure 1.8: Setup scheme of the time-delay compensated monochromator with all its optical components (adapted from [4]).

Indeed, it is possible to divide the monochromator in two identical section, each composed by two toroidal mirrors and one grating, divided by an intermediate slit that allows to select the harmonic that is requested for the measurement. The first section gives a spectrally dispersed image of the HHs (high-order harmonics) on the intermediate plane, closing the slit just one harmonic propagates toward the second section, where it happens both the temporal and spatial compensation, giving a spectrally selected stigmatic image on its focal plane. The first toroidal mirror is used as collimator and the second as condenser. All the four mirrors are at the same grazing angle and unity magnification in order to minimize aberrations effects, in particular the all the distances are the same:

- *Input arm*: is the distance between the HHs source and the vertex of the first toroidal mirror, and is equal to the distance between the slit position and the vertex of the third toroidal mirror.

- *Output arm*: is the distance between the vertex of the fourth toroidal mirror and the output focal point and it is equal to the distance between the vertex of the second mirror and the slit.

For all the mirrors the tangential and sagittal radii are the same and can be

expressed respectively as R and ρ from this two equations:

$$R = \frac{2p_M}{\sin\theta} \tag{1.51}$$

$$\rho = 2p_M \sin\theta \tag{1.52}$$

where θ represent the grazing angle of the toroidal mirrors and p_M represent the input arm of the collimator (or likewise the output arms of the condensers). The harmonic selection is given by the rotation of the gratings around an axis that is tangent to their vertex and parallel to the grooves. As said in the above section, it is possible to obtain the maximum of efficiency just at one input wavelength, and according to equation (1.50) it can be written as:

$$\lambda_B = \frac{2\sin\gamma\sin\delta}{m\sigma} \tag{1.53}$$

while at different wavelength respect λ_B the efficiency decreases due to the gratings that is working in off-blaze conditions. At the slit plane the spectral dispersion can be written as:

$$\frac{\Delta l}{\Delta\lambda} = \frac{m\sigma p_M}{\cos\beta} \approx m\sigma p_M \tag{1.54}$$

In order to select the n-th harmonics (obviously n is odd), and to assure that the $(n+2)$-th and $(n-2)$-th are filtered out the slit aperture must satisfy:

$$\Delta S_{H_n} = m\sigma p_M \frac{\Delta\lambda_{H_{(n-2)}-H_{(n+2)}}}{2} \tag{1.55}$$

where $\Delta\lambda_{H_{(n-2)}-H_{(n+2)}}$ describes the distances in wavelength between the harmonics $(n+2)$-th and $(n-2)$-th, and can be expressed as:

$$\Delta\lambda_{H_{(n-2)}-H(n+2)} = \lambda_0\left(\frac{1}{n-2} - \frac{1}{n+2}\right) \approx \lambda_0\frac{4}{n^2} \tag{1.56}$$

where λ_0 is the wavelength that is used to generate HHs. Applying this approximation to equation (1.55) the slit aperture is given by:

$$\Delta S_{H_n} = m\sigma p_M \lambda_0 \frac{2}{n^2} \tag{1.57}$$

The last condition that must hold in order to guarantee temporal compensation is that all the rays at different wavelengths, that compose the spectrum of the pulse after HHG, must be focused on the same point and with equal optical path. Assuming the FWHM of the spectral width of the n-th harmonics Fourier-transform limited, from equation (1.46) it can be obtained the width of the wavelength:

$$\Delta\lambda_{1/2,H_n} = \frac{1}{n^2} \frac{\lambda_0^2}{\Delta\tau_{1/2}} \frac{2.77}{2\pi c} \tag{1.58}$$

The rays must be focused on the same point because of the negative dispersion introduced by the second stage, so that the spectral dispersion at the output of the monochromator results zero. In this conditions it possible to achieve the goals fixed at the beginning of the dissertation, allowing to select just one harmonic without introducing any external perturbation that could change the property of XUV radiation.

Chapter 2

XUV Pulse Characterization

2.1 Introduction

High-order harmonic generation (HHG) is at the basis of many works which aim is to investigate those phenomena that occur on extremely short temporal periods. In the first chapter I treated how such harmonics can be generated and how it is possible to select just one of them in order to study the behavior of one physical system when it is subject to a given frequency. So temporal characterization becomes of main importance in order to analyze measurement results and to develop some models. For this reasons in this chapter I will discuss how this characterization process is done and which are the most common techniques. In particular this chapter is organized as follows: section 2.2 contains the theory behind pulse characterization, in detail *Frequency-Resolved Optical Gating for Complete Reconstruction of Attosecond Bursts* (FROG-CRAB) method will be discussed here, section 2.3 contains the practical implementation of FROG-CRAB with the description of the setup used for measurement, section 2.4 contains a brief description of the algorithm used for the pulse reconstruction and section 2.5 contains the experimental results obtained with the configuration described.

2.2 Theory of characterization

A possible way to characterize an XUV pulse is given by the analysis of the so-called *sidebands* (SB). When a monochromatic XUV pulse is focused on a gas (commonly noble gases are used), because of its high energy, it ionizes the atoms and generates free electrons called photoelectrons [25]. Those photoelectrons maintain the same temporal structure of the radiation that generates them, so the velocity at which they leave from the nucleus is proportional to the energy of the XUV pulse: the result is a line in the photoelectrons energy spectrum 2.1 because noble gases allows just one transition.

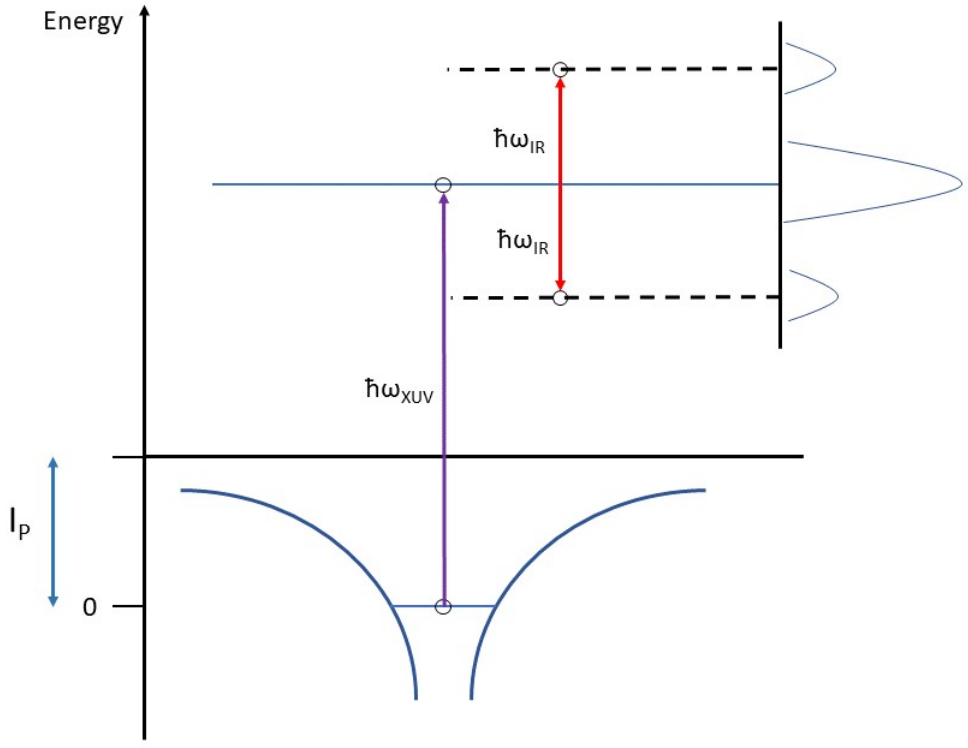

Figure 2.1: Scheme of sideband generation process

If the XUV pulse is spatially and temporally overlapped to an IR pulse the kinetic energy that is seen by the generated photoelectrons is different respect a non-overlapping case. In detail, if the temporal duration of the optical cycle

of IR is longer than the XUV pulse, the final momentum of the photoelectrons will follow the vector potential of the IR field. On the contrary, if the IR optical cycle is shorter than the XUV pulse sidebands are generated [26]. This phenomenon becomes visible considering a varying delay between the two pulses and acquiring the energy spectrum delay per delay. The result of this approach is the construction of a spectrogram: $S(\omega, \tau)$.

2.2.1 FROG-CRAB Technique

One of the most used techniques that allows to fully reconstruct an ultrashort XUV pulse is: *Frequency-Resolved Optical Gating for Complete Reconstruction of Attosecond Bursts* (FROG-CRAB) [12]. This approach is inspired by the *Frequency-Resolved Optical Gating* (FROG) [27] that consists of decomposing the pulse to be characterized in temporal slices making use of a temporal gate function $G(t)$ and then measuring the spectrum of each slice. This process is at the basis of the construction of a two-dimensional set of data called *Spectrogram* (also known as FROG trace), defined a:

$$S(\omega, \tau) = \left| \int_{-\infty}^{+\infty} dt\, G(t) E(t-\tau) e^{i\omega t} \right|^2 \tag{2.1}$$

where $E(t)$ is the field of the pulse that has to be characterized and τ is a variable delay between the gate and the pulse. The gate function can be either a given function related to the pulse (also the pulse itself is a suitable choice), or an unknown function (blind FROG). The FROG method operates in an iterative way: a spectrogram $\tilde{S}$ is computed starting from an initial guess $[E(t), G(t)]$.

$$\tilde{S}(\omega, \tau) = \int_{-\infty}^{+\infty} dt\, E(t) G(t) e^{i\omega t} = |\tilde{S}(\omega, \tau)| e^{i\tilde{\phi}(\omega, \tau)} \tag{2.2}$$

Given this simulated spectrogram, it is possible to pass to the second step, where the phase is conserved and the modulus $|\tilde{S}(\omega, \tau)|$ is replaced with the one given

by the measured spectrogram. So, the new simulated spectrogram becomes:

$$\tilde{S}(\omega,\tau) \longrightarrow \tilde{S}'(\omega,\tau) = \sqrt{I(\omega,\tau)}e^{i\tilde{\phi}(\omega,\tau)} \tag{2.3}$$

where $I(\omega,\tau)$ is the spectrogram experimentally measured. The third step consists in creating an error function defined as the difference between the experimental spectrogram and the one obtained by equation 2.3 so that thanks to a proper algorithm it is possible to determines a new pair of fields $[E'(t), G'(t)]$ used for the subsequent iteration. This process is repeated n times, until the algorithm converge when the error function is below a certain toleration value, and the final pair $[E^{(n)}(t)$,$G^{(n)}(t)]$ is obtained.

FROG-CRAB is based on photoionization of atoms or molecules thanks to the XUV pulse that has to be characterized; in addition of the XUV also an IR pulse, with variable delay τ with respect the first, is focused on the atoms, so that is possible to define a function that acts as the temporal gating for the FROG. FROG-CRAB was born with the goal of fully characterize attosecond pulses, so that kind of pulses has been extensively tested and investigated, anyway the applicability of this approach to few-femtosecond pulses has still to be proven, in particular, the narrower bandwidth associated with a single harmonic and the associated loss of sub-cycle resolution, reduces the level of information redundancy in a FROG-CRAB trace, so that it is necessary to develop a new approach to reconstruct also femtosecond pulses [5]. Assuming that holds the Strong Field Approximation (SFA), it is possible to write the spectrogram given by photoelectrons with kinetic momentum $\mathbf{v}$ at a generic delay instant τ, $S(\mathbf{v},\tau)$:

$$S(\mathbf{v},\tau) = \left| \int_{-\infty}^{+\infty} dt\, \mathbf{d}_{\mathbf{p}(t)} \cdot \mathbf{E}_x(t-\tau) e^{-i\Phi(t)} e^{i(W+I_p)t} \right|^2 \tag{2.4}$$

where

$$\phi(t) = \int_{t}^{+\infty} dt' \left[\mathbf{v} \cdot \mathbf{A}_{IR}(t') + \mathbf{A}_{IR}^2(t')/2 \right] \tag{2.5}$$

is a temporal modulation phase term.

- $\mathbf{d}_{\mathbf{p}(t)}$ is a dipole transition matrix element from the ground state to the continuum state $|\mathbf{p}\rangle$.
- $\mathbf{p}(t) = \mathbf{v} + \mathbf{A}_{IR}(t)$ is the instantaneous momentum of the free electron in the laser field.
- $\mathbf{E}_x(t)$ is the electric field of the XUV pulse, polarized along the x axis, so that $\mathbf{E}_x(t) = \partial \mathbf{A}_x(t)/\partial t$, where $\mathbf{A}_x(t)$ is the field vector potential.
- $W = \frac{1}{2}\mathbf{v}^2$ is the final kinetic energy.
- I_p is the ionization potential of an atom.

From equations (2.4) and (2.5) it is easy to notice that the input IR laser field introduces a temporal phase modulation $\phi(t)$ on the electron wave packet $\mathbf{d}_\mathbf{p} \cdot \mathbf{E}_x$ generated in the continuum by the XUV pulse. The interaction can be considered as a pure phase gate $G(t)$, so that the IR field is acting as an ultrafast phase modulator. In a more qualitative way, the electron trajectories, from the ionization instant to the spectrometer, can be considered as dependent on the electron time of ionization within the IR laser field optical cycle [28]: if the XUV pulse is longer than the optical cycle of IR pulse, then the final effect is a periodic phase modulation on the electron wave packet that causes the generation of additional peaks called sidebands (SBs) spaced by $\hbar\omega_{IR}$ respect the harmonic peak in the energy spectrogram of the photoelectrons. These sidebands are produced by the absorption of a harmonic photon and the additional absorption or emission of an IR photon as described in figure (2.1).

2.2.2 Simulations

Sidebands

In figure (2.2) is shown an image of the sidebands generated from the harmonic 25 that ionize an atom of Argon. The IR intensity used is $I_{IR} = 10^{11}\ W/cm^2$ for (a), while in (b) $I_{IR} = 10^{12}\ W/cm^2$. The temporal duration of the XUV and IR pulses are respectively $\tau_{XUV} = 5\ fs$, $\tau_{IR} = 10\ fs$ assuming both pulses to be transform limited.

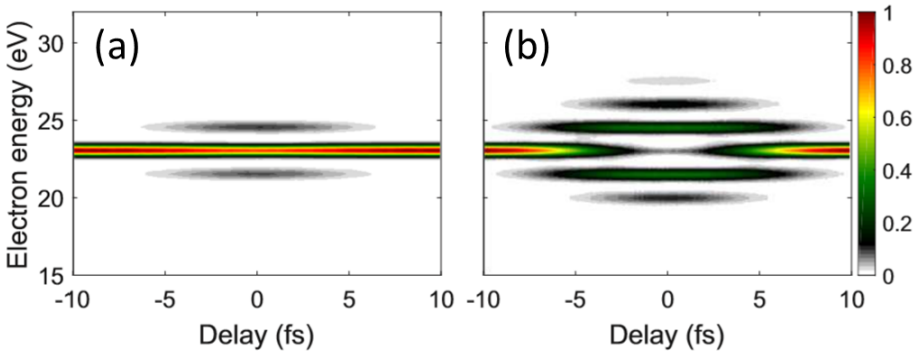

Figure 2.2: Spectrograms generated by HH25. In (a) the IR intensity was $I_{IR} = 10^{11}\ W/cm^2$, while in (b) $I_{IR} = 10^{12}\ W/cm^2$. This intensity difference becomes clear looking to the number of SBs generated, where in (a) IR is sufficient to generate just 2 sidebands, in (b) thanks to higher intensity 5 SBs are visible. The parameters used are: Argon as ionization gas, XUV and IR are assumed to be both transform limited, $\tau_{XUV} = 5\ fs$, $\tau_{IR} = 10\ fs$ (adapted from [5])

It is clear how the central line of the spectrogram, that describes the harmonic yield, is subject to a depletion when the XUV and IR pulses are spatially and temporally overlapped, in other words, when their delay τ is null. The sidebands generation is also proportional to the intensity of the IR pulse: the more it is intense the more it will interact with the photoelectrons generating more sidebands as shown in figure (2.2).

Chirped pulses

Another important information given by the sidebands analysis is the linear *chirp* (quadratic phase) of the pulse. The chirp is a phenomenon that describes

how frequencies, that compose a pulse, arrives at different time instants.

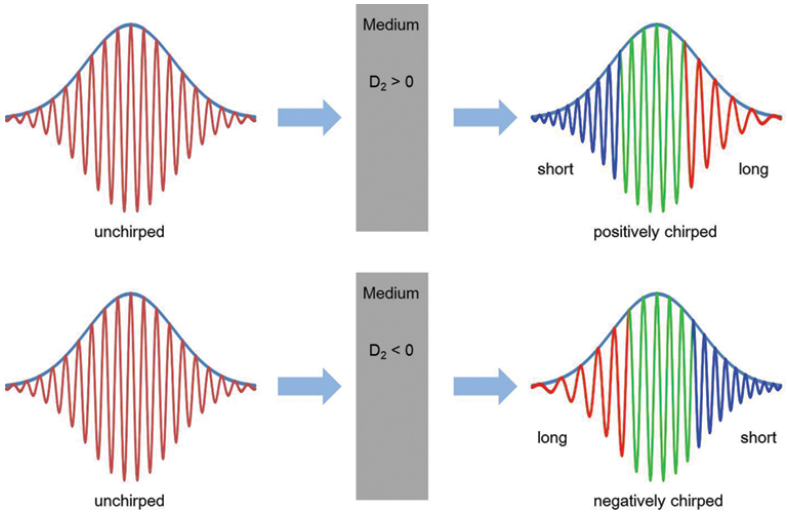

Figure 2.3: Frequency chirp after the pulse is passed through two different kind of mediums. In particular the first medium has positive D_2 (called second order dispersion, $D_2 = L \cdot \text{GVD}$, where L is the length of the medium and GVD is the Group Velocity Dispersion), so the higher frequency will come later then lowers. In the second medium, with negative D_2, it occurs the opposite respect the first case (adapted from [6]).

As shown in figure (2.3) in dependency of the medium that is traveled by the pulse, it is possible to describe two different behaviors that represent the chirp:

1. *Positive chirp*: *Group Velocity Dispersion* (GVD) is positive, so it means that the red component of the pulse has higher velocity respect the blue component, as a consequence lower energy is arriving before the higher one.

2. *Negative chirp*: GVD is negative, so the blue component of the pulse has higher velocity respect the red one: higher energies are arriving first, while lower energies later.

In the case of the spectrogram analysis, the chirp of the pulses is observed thanks to the tilt of the sidebands, where in particular it is possible to distinguish if the chirp is given by the IR pulse, by the XUV pulse or by both of them.

- The chirp on the harmonics pulse produces tilted SBs both with the same angle.

- The chirp on the IR pulse produces tilted SBs with opposite angles.
- The chirp on both XUV and IR pulses generates a sideband almost flat, and the other even more tilted: this effect is given by the superposition of the effects of the single XUV chirp and IR chirp.

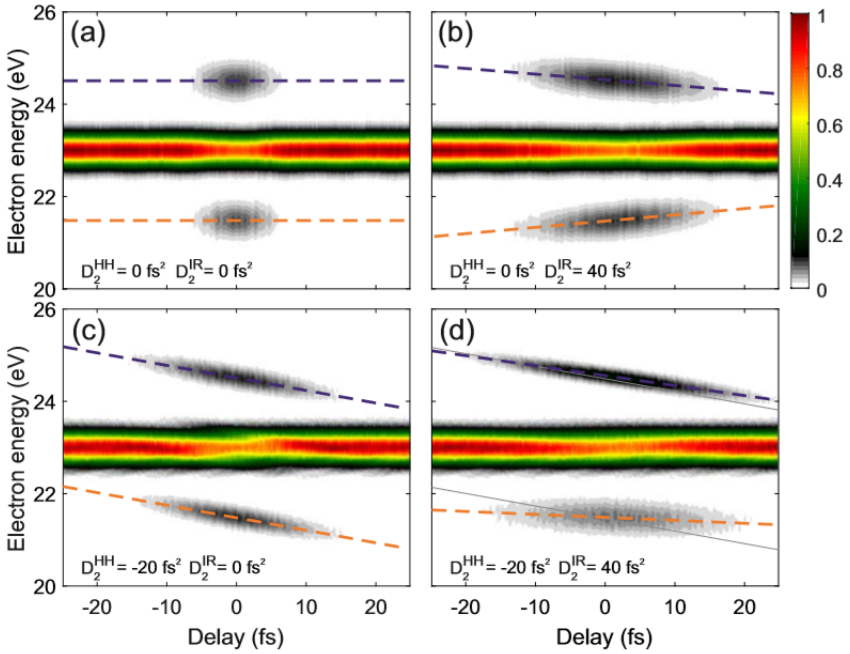

Figure 2.4: Effect of the IR and XUV spectral chirp on the HH spectrogram: in (a) it is represented the spectrogram of HH25 for transform limit (TL) pulse, (b) and (c) show the chirp of IR ($D_2^{IR} = 40\ fs^2$) and XUV ($D_2^{XUV} = -20\ fs^2$) respectively, and in (d) both the pulses are chirped. The dashed blue and orange lines represent the evolution of the SB center as function of the pump-probe delay. The XUV pulse has a temporal duration of 5 fs, and the IR of 10 fs with an intensity $I_{IR} = 10^{11}\ W/cm^2$. The gas used for ionization was Argon. (adapted from [5])

2.3 Experimental Setup

Generation and characterization of XUV pulses is a process that requires a complex setup, that can be schematically divided in 4 steps:

1. Pulse compression
2. High-order Harmonic Generation
3. Harmonic selection

4. Harmonic characterization

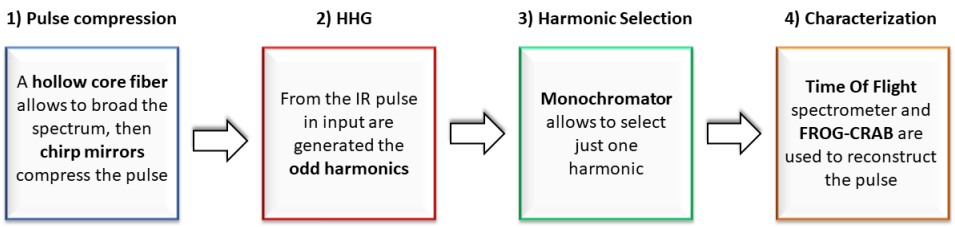

Figure 2.5: Scheme of the 4 steps necessary to the measurement process

In order to provide a complete description of the entire setup, for each step written above, I will evidence the elements that we have used to assemble it, underlining the main characteristics, and where it is necessary also the theoretical parts.

2.3.1 Pulse compression

This is the first step, and consists of all those elements that allow to generate an ultrashort high-intense pulse that will be used to obtain high-order harmonic generation.

Laser Source

The laser source used is a commercial Astrella produced by Coherent. Its active medium is a crystal of Ti:Sapphire water cooled and it is designed to provide up to 7 mJ pulses energy at a repetition rate of 1 kHz, a wavelength of 800 nm and pulses temporal duration shorter than 35 fs. A peculiarity of this laser source is its stability ($< 0.5\%$ rms) that allows to get high-quality measures, without the presence of any significant variation in pulse intensity.

Stabilization

So an IR ultrashort pulse (around 35 fs) is given in output from the laser source.

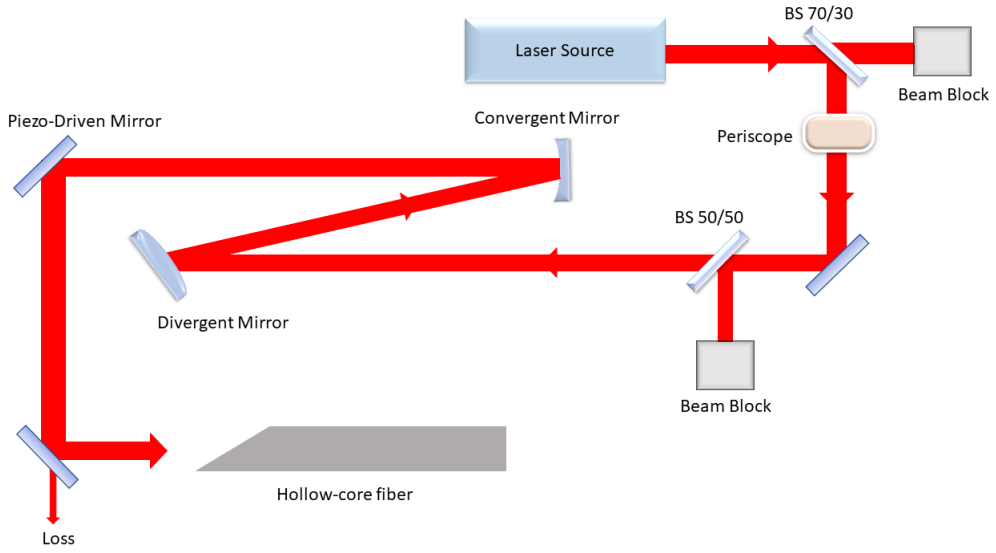

Figure 2.6: Scheme of the setup before the hollow-core fiber

At this moment the pulse has a power of 7 W that is too much for our intent, so, as it is possible to see in figure (2.6), a 70-30 beam splitter (BS) is used to reduce the intensity of the pulse: the 30% reflected is taken, while the other 70% that passes trough the BS is not used and is blocked. The part of beam that is reflected, than goes to a periscope that lowers it from the laser output height (16.3 cm) to the optical elements height (8.8 cm). Then another beam splitter (50-50 BS) is used to reduce again the intensity of the pulse, in order to achieve around 1 W. Now the correct pulse intensity is achieved, so the beam must be focus to the fiber entrance (the fiber will be discussed in the next paragraph). For focusing we decided to use spherical mirror instead of convergent/divergent lens, because when the pulse passes trough the lens causes third order non-linear phenomenon as self-phase modulation that produce a bandwidth broadband that, in this part of the setup, is better to avoid. So, the first spherical mirror is divergent with a curvature radius of +4000 mm, while the second is placed

after 60 cm and is convergent with a curvature radius of -2500 mm. The ABCD matrix of the system is determined so that the focal distance is around 2.35 m. After the focusing part, the beam goes to a 45° dielectric mirror that is mounted on a piezoelectric motor used to stabilize the direction of the pulse. Then the beam goes to another 45° dielectric mirror with high reflectivity (around 99.9%) that direct the pulse to the hollow fiber. The loss of the dielectric mirror (less than 0.01%) is used for the stabilization block that is so composed:

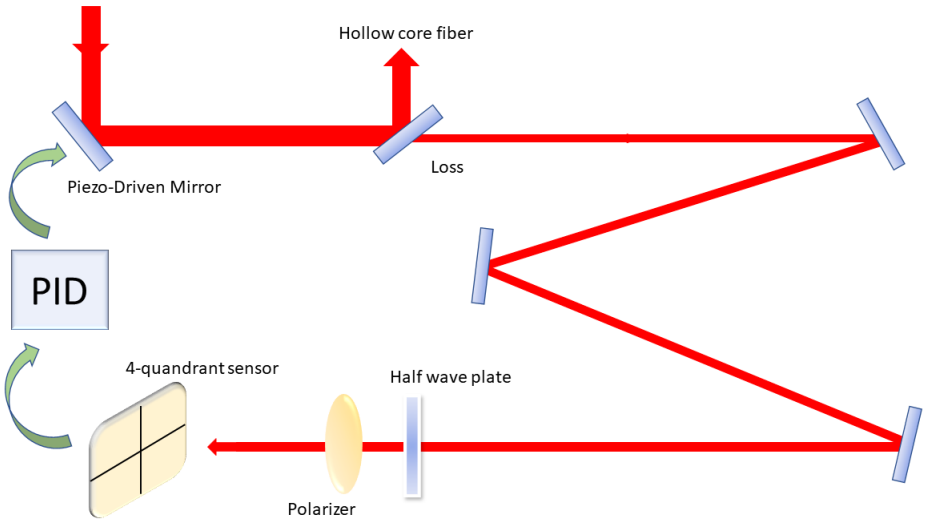

Figure 2.7: Stabilization scheme before the hollow-core fiber.

The stabilization block consists of a half wave plate, followed by a polarizer, a four quadrants sensor and a *PID* (Proportional-Integrative-Derivative) controller inserted in a retroactive system. The loss of the pulse is centered, thanks to folding silver mirrors, in the middle of the four-quadrant sensor. In order to avoid sensor's saturation, we have to attenuate the pulse and it is necessary to use first a half wave plate then a polarizer, as shown in figure (2.7). The attenuated signal is seen on the sensor that determines the horizontal and vertical position of the beam.

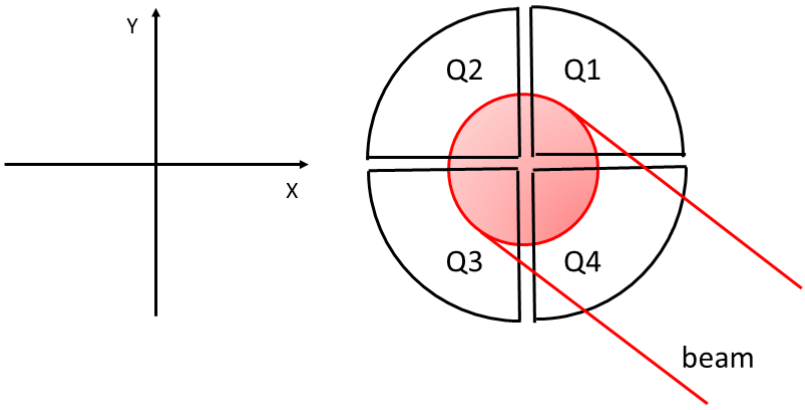

Figure 2.8: Scheme of the four-quadrant sensor: the beam impinges on the sensors, and each of them collects a certain intensity value, then, comparing each quadrant's detected intensity, it is possible to know the x and y coordinates of the beam respect the center

The measured x and y indicate the position of the beam; these values are sent to a PID controller that compensates for any beam displacement acting on the dielectric mirror that is mounted on the piezoelectric as shown in figure (2.7). PID controller is an important element used in automatics control that allows to eliminate deviations with respect to a given value when it operates in a closed-loop regime. Its action is on 3 different levels:

- *Proportional action*: the output compensation signal is obtained by the product of the error signal $e(t)$ obtained by the subtraction between the input signal and the output of the process times a proportional constant K_p defined by the PID parameters, so it gives a proportional contribute to the total action:

$$u_P(t) = K_P\, e(t) \tag{2.6}$$

- *Integrative action*: the output compensation signal is obtained by the integral of the error, multiplied by an integration constant K_I; in this case the controller "has memory" of the past events, so the action corresponds

to a mean process of the error and it compensates for slow variations:

$$u_I(t) = K_I \int dt\, e(t) \tag{2.7}$$

- *Derivative action*: the output compensation signal is obtained by the the derivate of the error, multiplied by a derivation constant K_D; in this case the idea is to compensate for fast variations, so that if the error grows the controller acts immediately to reduce the impact:

$$u_D(t) = K_D \frac{de(t)}{dt} \tag{2.8}$$

The sum of equations (2.6),(2.7),(2.8) gives the complete action of the PID:

$$u_{TOT}(t) = K_P\, e(t) + K_I \int dt\, e(t) + K_D \frac{de(t)}{dt} \tag{2.9}$$

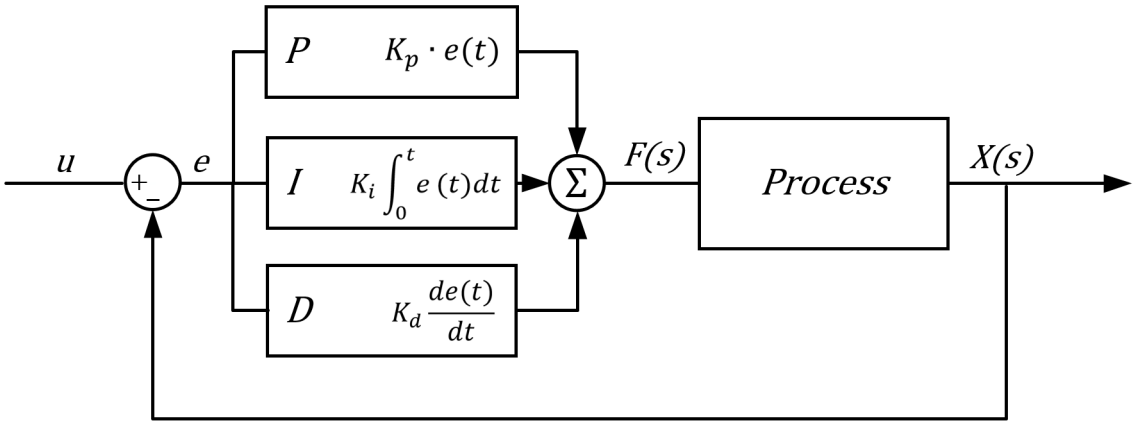

Figure 2.9: Block scheme of a PID controller

The signal obtained by equation (2.9) is sent to a piezoelectric that consequently moves the dielectric mirror that compensates for any beam displacement related to any optical elements described before and those that are internal to the laser source. This process of stabilization is of fundamental importance because the fiber entrance is in correspondence of the laser focal point, so it is really

energetic and if the beam would be free to randomly drift (even few μm) it could damage the fiber itself, then the output mode would change significantly, so the complete measure would be ruined.

Hollow-core fiber

The hollow-core fiber is a fundamental element of this setup, and it allows to obtain a pulse with spectral broadening. In our case the fiber is composed by a small tube of glass, it is long $\approx 1\ m$ and it has an internal diameter of $\approx 300\ \mu m$. This diameter is an upper bound for the diameter of the beam, indeed, in order to achieve the maximum of coupling factor it should be the 3/2 of the FWHM of the beam itself.

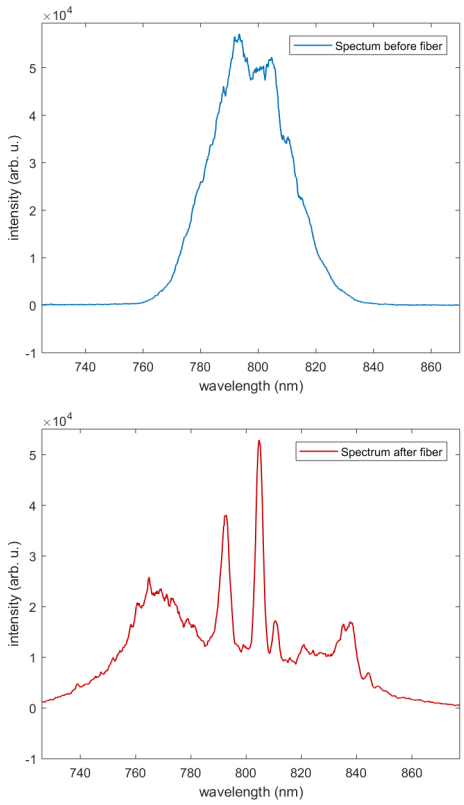

Figure 2.10: In the blue image it is shown the spectrum of the IR pulse before the hollow core fiber, while on the red is shown the spectral broaden related to the Self-Phase Modulation (SPM).

As said above, the goal of using the fiber is to obtain a pulse with larger spectrum, and this happens when the core is filled with a noble gas, in our

case neon has been used. The interaction between the laser pulse and the gas produces a third-order non-linear effects called *Self-Phase Modulation* (SPM). This phenomenon is related to a variation of the reflective index of the gas that acts as a Kerr medium. This implies that the reflective index is a function of the intensity of the field, so the pulse receives an auto-induced modulation of the phase that will broaden the spectrum of the pulse itself. The SPM generates new frequencies, so that it allows to obtain a shorter transform-limited pulse (the larger is the spectrum the shorter is the temporal duration of the transform-limited pulse). A homogeneous broadening is achieved using a single mode guiding structure, but the commonly used optical fibers have small energies tolerances (just in the order of nJ). In our case, we needed higher input energies (around 1 mJ). For this reason the choice of a hollow-core fiber has been necessary, even though, in this case, the propagation is no more owed just to total internal reflection but the fundamental mode is selected depending on losses: the one with lower losses is the mode taken. The quantity of losses inside the fiber is related to the gas pressure. A series of repeated experiments has demonstrated that, for our purpose, the optimal gas pressure to use is around 0.8 bar, because in this condition:

- The output pulse has a power of 820 mW, and considering that the input power was 1 W, we are able to achieve an efficiency $\eta = P_{output}/P_{input} = 82\,\%$, that is extremely a good result.
- An analysis of the spectrum evinces that the transform-limited pulse duration is under 10 fs, that is a good value both for starting generating HHs and to get the shortest possible pulses after the monochromator.

As the pulse exits from the fiber, it has a large spectrum and is quite long (around 35 fs), so it must be compressed to achieve the pulse duration necessary to generate HHs. There exists many techniques that allow to obtain so short

pulses, but one of most efficient is the use of *chirped mirrors*. Their working principle is quite easy to understand: the beam, that is composed by many wavelengths (here the pulse has a broad spectrum), impinges on the chirped mirror, made by the superposition of many layers that with proper reflective indexes generates constructive/destructive interference in the field's components, introducing a negative GVD. This process is schematically represented in figure (2.11).

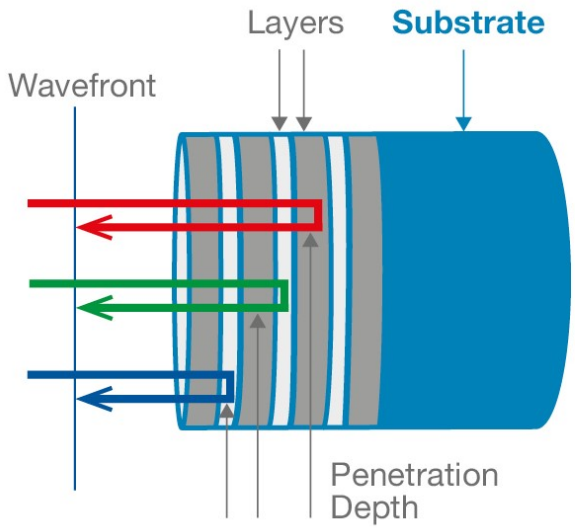

Figure 2.11: Schematic representation of a chirped mirror (adapted from [7]).

In our setup we used the chirped mirrors in order to introduce negative D_2 and achieve a pulse duration of around 10 fs. The setup is shown in figure (2.12). After the pulse compression, the beam is split thanks a 80-20 BS: one part is centered to the entrance of the chamber for HHG, while the other is sent to a variable delay line and is used as probe for the characterization measurement. At the end of the pulse compression stage we obtain an ultrashort high-intense peak pulse that is able to generate harmonics in an efficient way.

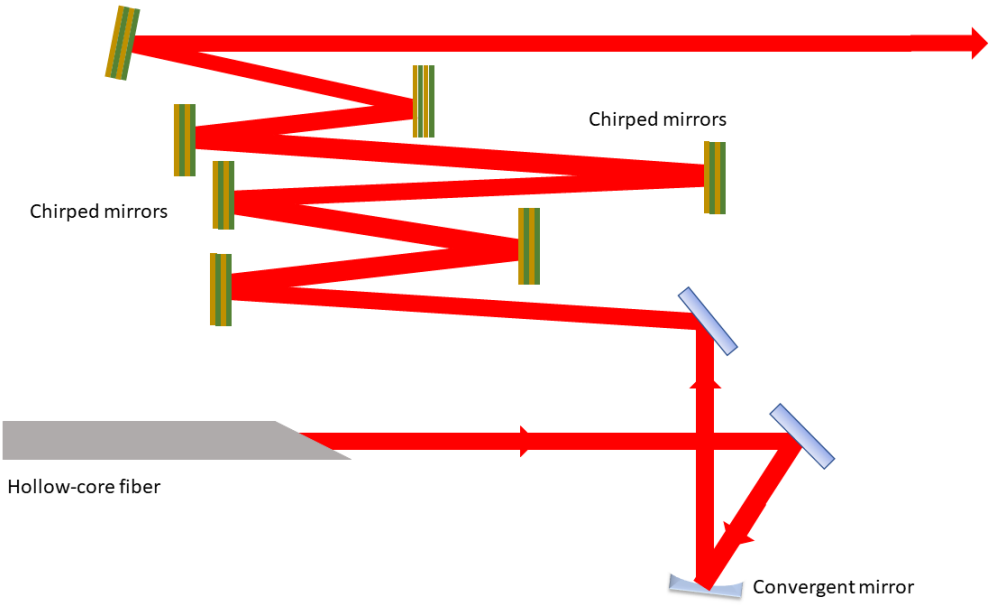

Figure 2.12: Scheme of our chirped mirrors setup. After the fiber the pulse is focused thanks a convergent mirror of radius $R = -3000\ mm$, then seven chirped mirrors introduce a negative dispersion that allow the pulse compression. After this stage the temporal duration of the IR beam is around 10 fs. After this stage the pulse is ready to be used to generate HHs.

2.3.2 High-order Harmonics Generation

In Chapter 1 it has been described how high-order harmonics generation happens under two theoretical points of view, one semiclassical, the other quantum mechanic based. In this section I will describe just how we obtained such harmonics with the setup used. First of all the pulse enters inside the chamber used for generation passing through a flange at Brewster's angle in order to avoid reflections losses, then is sent to a convergent spherical mirror with a curvature radius of $-750\ mm$ in order to focus the beam on the cell for HHG. The cell is a block of metal drilled with a hole long 1 cm and with a diameter of 0.3 cm where the gas is inserted. The two sides of the hole are both covered with aluminum tape. When the field arrives on the cell, it drills a circular hole in the aluminum tape, interacts with the gas and generates HHs. The gas used depends on the harmonics we want to obtain, indeed as seen in Chapter 1 the cut-off frequency

depends on the ionization potential of the gas: in a simple approximation Argon is used to generates harmonics highly energetic (it is possible to reach the 31-th order), while for lower energetic harmonics (9-th order) we used Xenon. The chamber kept in high vacuum regime, both during generation ($\approx 10^{-3}\ mbar$) and non generation ($\approx 10^{-7}\ mbar$).

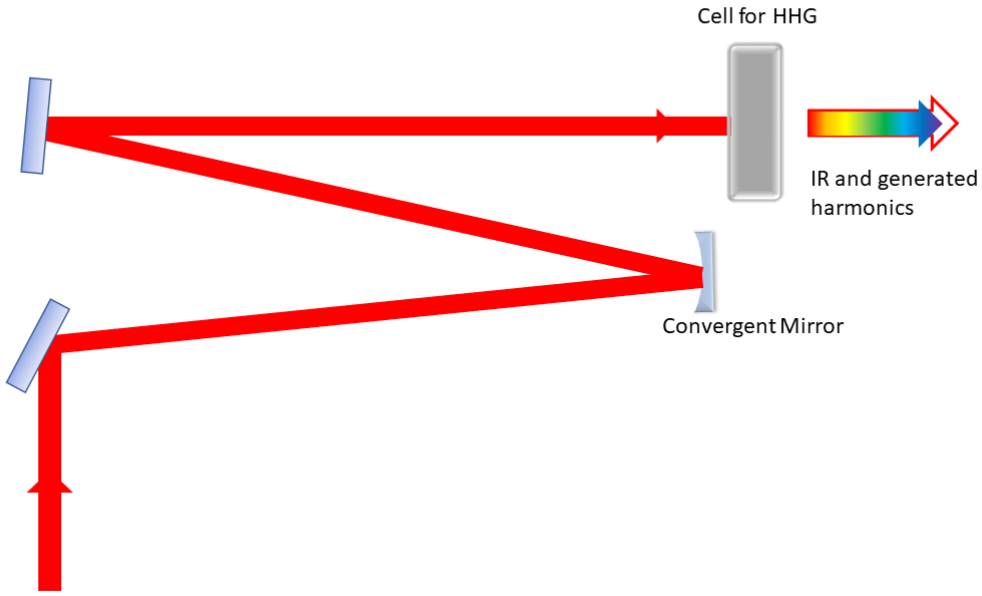

Figure 2.13: Scheme of the generation chamber used in our setup

2.3.3 Harmonic selection

As discussed in Chapter 1 the selection of just few harmonics is of crucial importance in order to realize different kind of experiments. We used a time-delay compensated monochromator with the following characteristics:

- All the toroidal mirror have the same length of 50 mm and height of 10 mm.
- The sagittal radius is of 31.50 mm for all the toroidal mirrors.
- The first toroidal mirror and the last have a tangential radius of 18 mm,

while the second and the fourth have the tangential radius of 14 mm.

- The incident angle of the beam is always equal to 87.4°, while the acceptance angle is equal to 6.2 $mrad$.
- The input arm of the first toroidal mirror and the output arm of the fourth are long 364 mm, while the output arm of the second and the input arm of the third are long 340 mm
- The plane gratings are characterized by a groove density $\sigma = 400$ $grooves/mm$. They have a length of 30 mm and a height of 5 mm.
- The blaze angle is equal to 3°.

So the pulse enters in the chamber where is contained the time-delay compensated monochromator. As initial condition we consider that the gratings are all placed at zero order, and the selection slit is completely open in order to let the pulse pass through with all its spectral components. Then, it requires an optimization process before selecting the desired harmonic, indeed the counts we get at XUV detection, must be sufficiently high: so, first of all the position of the cell inside the generation chamber is adjusted, then the pressure of the gas, the intensity of IR beam that is used to generate HHs, and also the compression of the initial pulse acting on the hollow-core fiber. After this process, the wanted harmonic can be selected: with a Matlab program we can control the motors that rotate the gratings, so that the first diffraction order of the selected harmonic is focused at the center of the slit. Closing the slit we let just one harmonic passing to the second stage. Now also the gratings of this second stage can be rotated, so that the harmonic results optimized with the maximum output power. If a harmonic change is necessary, first of all, one should set the zero order in the second stage, fully open the slit, then changes the position of the gratings of the first monochromator, such that the new desired harmonic can be optimized.

If necessary, another optimization process (change the gas pressure inside the generation chamber) could increase the output power, and enhance the quality of the signal. At the end of the first monochromator there is an Al-filter, used to stop the IR beam when the order of the monochromator is both set at zero for the first and second stage, so no particular harmonic is optimized.

2.3.4 Harmonic characterization

This is the step where measurement is taken. It is the most sensible part of the setup, in the sense that even small perturbation could generates error in the alignment between the pulses, or changes in the temporal superposition. This part of the setup is composed by many elements that allows to successfully complete the measurements process.

IR delay line and overlap

As said above, before the IR pulse enters in the chamber to generates HHs, it is split such that one part of the IR pulse is centered in the generation chamber, while the other is reflected back in order to be used as probe during the characterization process. This reflected IR pulse is sent to a delay line. This delay line is composed by high precision carriage over which is placed a piezoelectric driven slit that moves two silver mirrors arranged in a proper way (so that the beam goes away parallel to the incoming direction) shown in figure (2.14). The piezoelectric is driven by a LabVIEW program that communicates how it must move in order to complete a full scan of the delays.

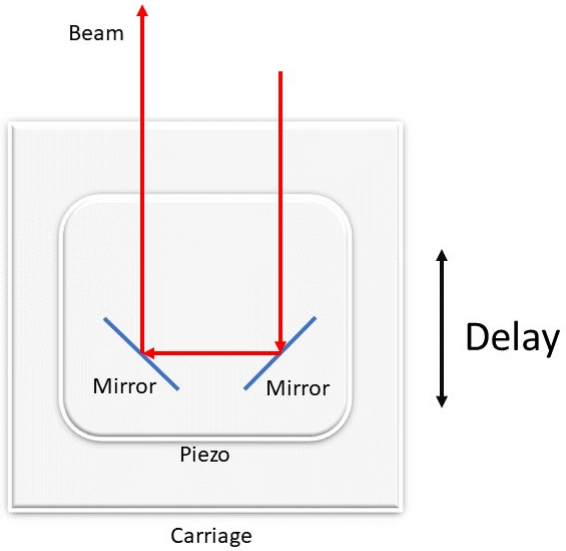

Figure 2.14: Scheme of the delay line: the piezoelectric is mounted over the carriage, and it moves the mirrors placed above, driven by the LabVIEW program

After the delay line the pulse is sent to a periscope that raises the beam to the height of the entrance to the chamber that contains the second grating. Indeed, in this chamber it takes place the recombination of the two pulses, IR and XUV (the selected harmonic). The beam enters in this chamber passing through a flange at Brewster's angle in order to reduces and avoid reflection losses. In order to get the overlap between XUV and IR pulse a collinear setup has been realized. The two beams are made collinear thanks to a drilled mirror: after the monochromator stage the selected harmonics has a small spot size (because it converging and the XUV divergence is small) that can pass through the hole of the drilled mirror, while the dimension of the IR field is much larger and can be reflected by the mirror. We took advantages of this fact, so, to obtain collinear overlapping we realized the setup shown in figure (2.15)

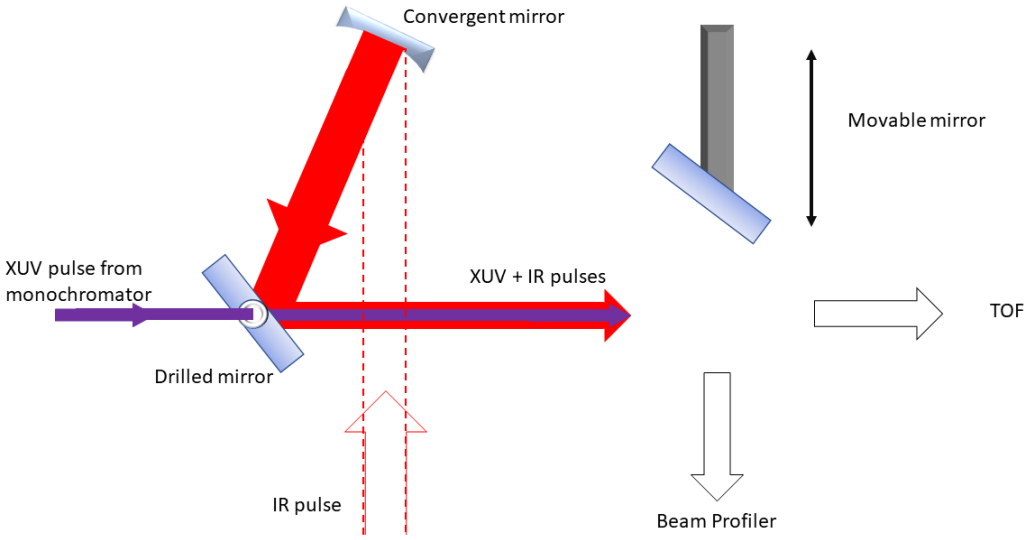

Figure 2.15: Scheme of the collinear overlapping setup. The XUV pulse is focused by the monochromator, so its spot size is smaller than the IR's. The XUV passes through the drilled mirror, while the IR is reflected. From now on the two beams proceed together: if the movable mirror is inserted they go on a beam profiler, else they enter in the time of flight (TOF) spectrometer.

In this configuration just a portion of the IR pulse is used to obtain the characterization, but anyway this collinear configuration is quite simple to be realized and correctly align, and in order to obtain the sidebands, a perfect spatial and temporal overlapping between IR and XUV pulses is essential. To be sure of the goodness of these superpositions, we used a collinear configuration that gives acceptable results in term of intensity and temporal duration. To verify the overlapping, we introduced a mirror after the drilled mirror of figure (2.15), so that the pulse instead of going to the TOF spectrometer, is sent to an external beam profiler. Of course in order to see the superposition, the time-delay compensated monochromator must be set at zero order, such that the IR pulse from the XUV path could interact with the IR from the delay line; then we will assume that changing the order will not affect the beam position. Spatial overlapping is achieved fixing on the beam profiler the peak position (x and y) of the IR pulse coming from the XUV line, keeping closed the IR from the delay

line. Then we close the XUV line and open the delay line, so we are able to center this pulse at the same peak position of the other. Temporal overlapping is more complex to achieve: first of all, perfect spatial superposition must be found, then one have to slowly manually move the carriage of figure (2.14), changing the optical path (so the delay) until an interference pattern appears. At this point, we can remove the mirror and start the acquisition process.

Time Of Flight Spectrometer

A Time-Of-Flight (TOF) spectrometer is a tool that is able to determine the energy of electrons (or ions), measuring the time that passes from the ionization to the detection. It is made by a cylindrical metal body, where at an extremity is placed a needle that injects the gas inside the TOF: in proximity of this needle, photoelectrons are generated thanks the interaction between the XUV pulse and the gas. As discussed previously this photoelectrons hold the characteristics of the XUV field, so they can be used to determine the pulse duration. The gases used to characterize the pulse are often noble gases because we need to have just one transition in order to avoid additional structures in the spectrum.

Generated photoelectrons are then accelerated by the IR pulse and focused by an electrostatic lens on a diffusion area, in our case, in order to detect even single electrons, we used a Micro-Channel Plate (MCP) detector. After the MCP, a detector counts how many electrons arrive at a certain time. In order to have a correct time detection, the TOF needs to be synchronized with an external trigger, that in our case is a photodiode placed behind one mirror after the hollow core fiber, that sends an electrical signal each time that the pulse is detected. The TOF is connected to a *Time to Digital Converter* (TDC), so that it is possible to measure the time requested by the electrons to cross the diffusion area. Electrons' energy is correlated with this temporal value, indeed electrons with different energies arrive at different time instants. In particular it

holds the relation:

$$E_{kin} = \frac{1}{2} m_e v^2 = \frac{1}{2} \frac{m_e L^2}{t_f^2} \tag{2.10}$$

Where L is the length traveled by the electrons inside the TOF, starting from the interaction area between the pulse and the gas, to the detection area, m_e is the electron mass and t_f is the time of flight, given by the formula:

$$t_f = \sqrt{\frac{m_e}{2Ve}}\, L \tag{2.11}$$

Where V is the difference of potential inside the TOF. Knowing V it is possible to retrieve the time of flight and consequently the energy.
For our measurements, the TOF was set in electrons mode, and data acquisition was managed by a custom-made LabVIEW VI, that determines: the integration time, the movement of the piezoelectric (figure 2.14) equivalent to a delay step, the total scan duration and many other parameters. This VI is also able to show the spectrogram obtained (2.16).

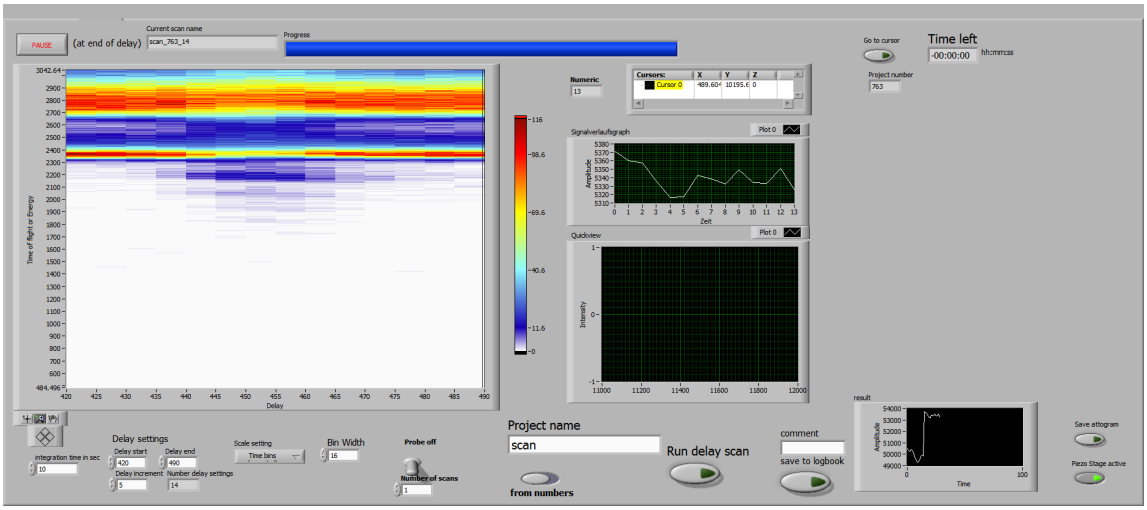

Figure 2.16: LabVIEW program used, properly adopted for our scope. There are shown the required parameters that determine the scan duration, the scan saving settings and the spectrogram defined by the photogenerated electrons detected and the relative delay.

Harmonic detection

After the TOF spectrometer, the harmonic that generates photoelectrons can be detected in order to do spectral analysis. For this reason we used a spectrometer composed by:

- Toroidal mirror, similar to the one used inside the time-compensated monochromator, that collimates the incoming field to the grating.
- Plane grating, with variable line spacing (VLS), that separates spatially the different spectral components of the beam.

After the monochromator the beam is sent to a Multi-Channel Plate (MCP), where the signal is amplified. The output electrons are accelerated and hit a phosphor screen, such that they can be detected with a CCD camera, revealing the harmonic spatial position. The spectrometer must be properly align with the harmonic pulse that is wanted to be analyzed, for this reason the camera is placed on a movable transition stage. The CCD acquisition data is managed by a LabVIEW VI, that is custom-made for our purposes. The result of harmonics detection is so shown in figure (2.17). To detect these three harmonics we set the monochromator at zero order so that gratings act as mirrors and spatial dispersion does not occur and slit is completely open.

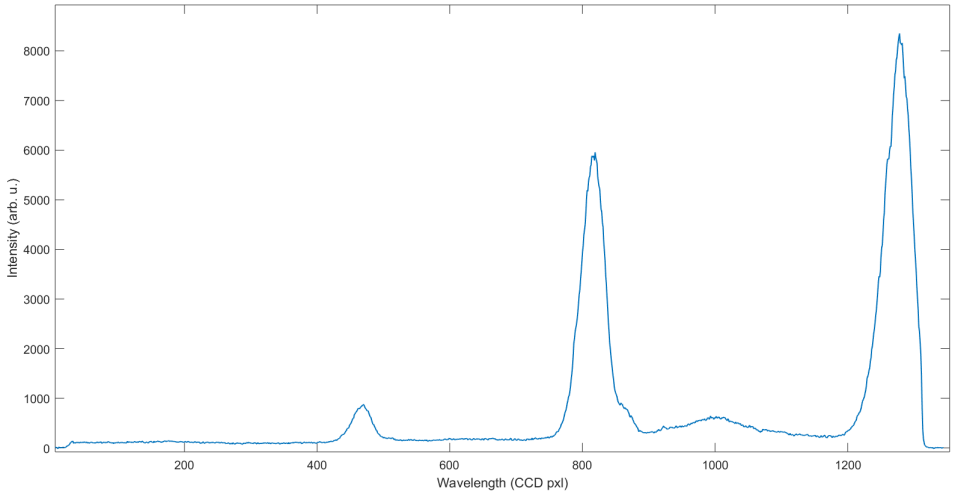

Figure 2.17: Representation of the generated harmonics. In particular, here are shown from left to right H13, H11 and H9.

The main parameter to control are the voltages applied to the MCP and to the phosphor screen; their values are not fixed, but they must be adjusted in order to avoid the saturation of the CCD.

2.4 Ptychographic reconstruction

The experimentally measured spectrogram $S(\mathbf{v}, \tau)$ (equation 2.4), is a real positive quantity, so by consequence the informations on the phase are completely lost. Different algorithms have been proposed with the intent to reconstruct the phase associated with Single-Attosecond Pulse (SAP) spectrograms [29], [30], [31]. Among all the prospected algorithms the extended Ptychographic Iterative Engine (ePIE) has shown better degree of convergence and robustness [32], [33], indeed in this kind of algorithm the delay and energy axis are not linked by a Fourier transform, so this relaxes the need for data interpolation. In addition, the code is sensitive not only to the relative time step, but also to the absolute value of the delay, so it can even operate with non equidistant sampling. Since ePIE cycles on each individual time delay step, a complete scan corresponds to

several algorithm iterations making it less subject to white noise and quicker in convergence. Also other algorithms as the Principal Component Generalized Projection Algorithm (PCGPA) and the Least Squared Generalized Projection Algorithm (LSGPA), that are efficient for attosecond pulses, have been tested, but for few-femtosecond they provided non adequate results as shown in figure (2.18): here there are shown the simulated and reconstructed spectrograms of HH25 selected from a 7.5 fs comb. In particular the first column shows the simulations, while the second the reconstructions obtained respectively with the PCGPA and the LSGPA.

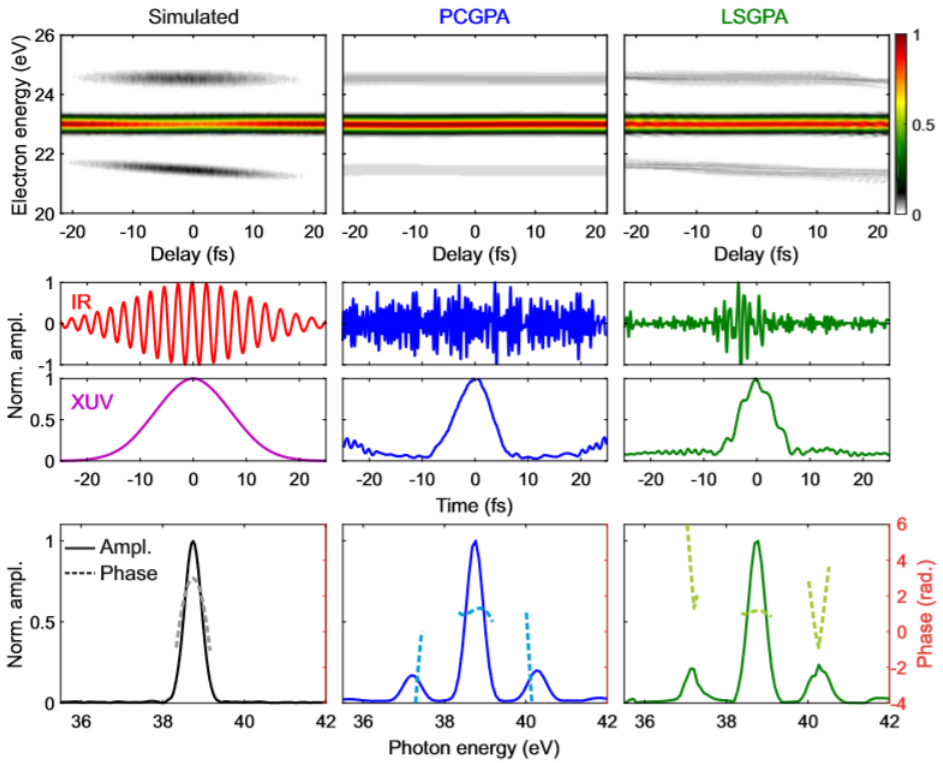

Figure 2.18: Examples of FROG-CRAB reconstruction with PCGPA and LSGPA. The first column shows the simulated data, the second and the third respectively PCGPA and LSGPA methods used to reconstruct the data. For each column, from the top to the bottom are represent: the spectrogram, the temporal behavior of IR and XUV (HH25), the spectral amplitude (solid) and the phase (dashed). For the simulation the following characteristics have been used:$\tau_{XUV} = 7.5\ fs$, $\tau_{IR} = 15\ fs$, $D_2^{XUV} = -20\ fs^2$, $D_2^{IR} = -60\ fs^2$ and $I_{IR} = 10^{11}\ W/cm^2$ (adapted from [5]).

As it possible to see these two methods fail in the attempt to reconstruct the correct IR, and both underestimate the time duration of the pulse. Also

the application of the ePIE algorithm can be quite critical, in particular when noisy experimental data are collected, or when small delay windows plus a bad energy resolution has been adopted. In order to improve the convergence, without increasing the to much the sampling time, we modified the ePIE code. At each iteration we added:

- A mobile average (smoothing) of the reconstructed XUV time phase: this is necessary to reduce the numerical high-frequency noise.
- An amplitude filter, as a super Gaussian: it is used to set at zero the XUV field at the boundaries of the time window where numerical reflections can occur.

Without this two considerations the algorithm would still converge, but the obtained solutions could be completely unphysical.

Then we tested the convergence of the ePIE approach applying it to a simulated spectrogram calculated by equation (2.4), assuming as input harmonic the 25-th, and ionized atoms of Argon. In particular, in figure (2.19) the first two columns show the simulated and reconstructed spectrograms, the third displays the XUV spectral phase and amplitude and last column shows the input and reconstructed IR pulse. We considered four different cases for the application of our algorithm: In the first row, we applied the ePIE algorithm to a transform-limited (TL) pulse, in the second row to a chirped XUV pulse with a $D_2^{XUV} = -20\ fs^2$, in the third row to both XUV and IR chirped pulses with $D_2^{XUV} = -20\ fs^2$ and $D_2^{IR} = -60\ fs^2$; this three simulation were done with an IR intensity of $10^{11}\ W/cm^2$, while the fourth, that is represented in row 4, has been taken with an IR intensity of $10^{12}\ W/cm^2$, and this fact can be seen by the higher number of sidebands on the spectrogram. The time durations of the pulses are $\tau_{IR} = 15\ fs$ and $\tau_{XUV} = 7.5\ fs$, and are the same for all the simulations. The sample temporal step used was of 2 fs, and reconstruction

runs over 2000 iterations.

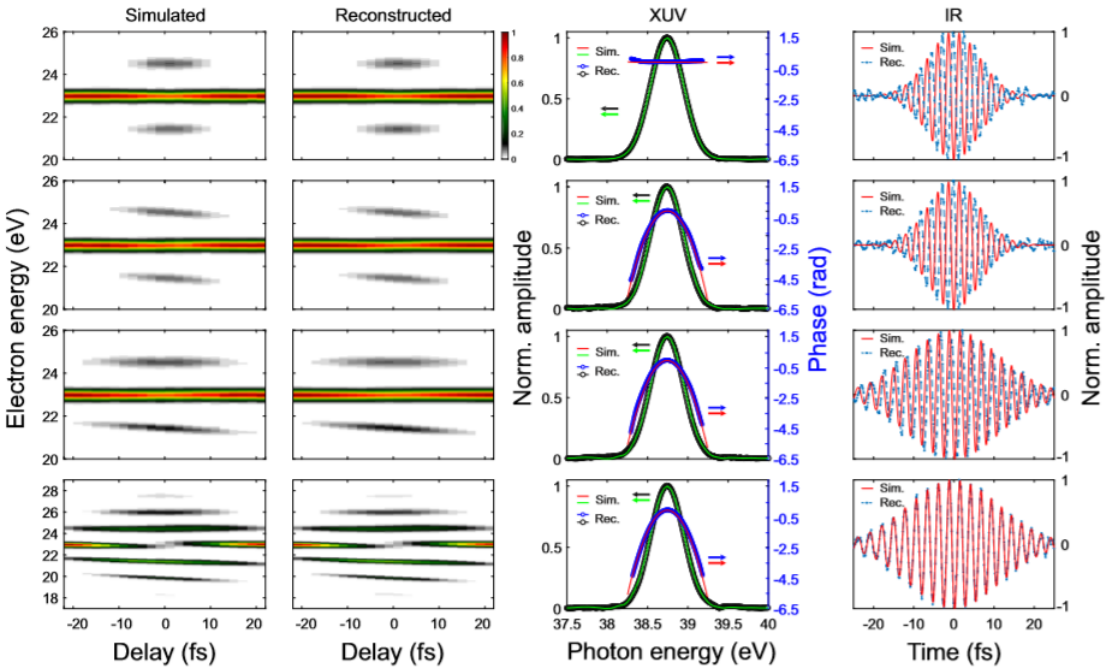

Figure 2.19: Example of ePIE algorithm: the first two columns show the simulated and reconstructed spectrograms, while the third and the fourth display the simulated and reconstructed XUV and IR pulses. In the first row it has been considered a TL pulse, in the second a chirped XUV with $D_2^{XUV} = -20\ fs^2$, in the third both IR and XUV are chirped with $D_2^{XUV} = -20\ fs^2$ and $D_2^{IR} = -60\ fs^2$, in the last row the two pulses are still chirped as in row 3, but the IR intensity has been increased from $10^{11}\ W/cm^2$ to $10^{12}\ W/cm^2$. The time durations $\tau_{IR} = 15\ fs$ and $\tau_{XUV} = 7.5\ fs$ are the same for all the simulations. The sample temporal step used was of 2 fs, and reconstruction runs over 2000 iterations. (adapted from [5])

2.5 Measurement Results

The setup that has been described in section 2.3 is then used to obtain the XUV photon spectrometer, then the ePIE algorithm described in section 2.4 has been applied. The temporal response of the monochromator has been determined considering two effects:

1. Compensation of the pulse-front tilt due to diffraction: when all the rays with the same wavelength emitted in different directions by the HHs source travel the same optical path. The optimal compensation is achieved for a

double-grating configuration, in other cases aberrations could give some distortion of the pulse-front.

2. Group Delay Dispersion (GDD) introduced by the time-delay compensated monochromator, that can be considered a XUV pulse shaper that introduces a controllable group delay dispersion, indeed the optical path decreases linearly with the wavelength and it forces the GDD to be constant and positive. In our case, with the given parameter of the time-delay compensator monochromator, we obtained $GDD_{HH19} = 20\ fs^2$ and $GDD_{HH27} = 7\ fs^2$

High-order Harmonic 27 and High-order Harmonic 19 reconstructions are shown in figure (2.20).

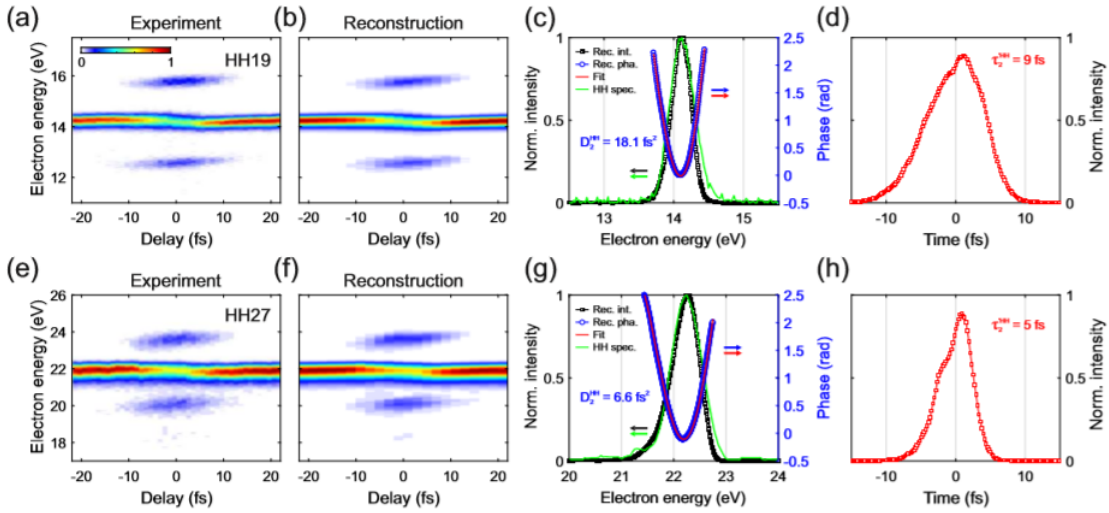

Figure 2.20: Example of application of ePIE algorithm to experimental results. Two harmonics have been analyzed, the 27-th in the first row and the 19-th in the second row. In the first column are shown the experimental spectrograms, in the second the reconstructed, in the third are displayed the experimental and the reconstructed harmonic amplitude (respectively green and black dot) and phase(red and blue dot), in the fourth it is shown the pulse reconstruction in time (adapted from [5]).

After only 2000 iterations of the algorithm we obtained very good results, in agreement with the experimental spectrograms. Another proof of the goodness of the algorithm's convergence is given by the comparison between the spectrum measured with XUV spectrogram and the one reconstructed with the algorithm

(fig. 2.20(c), fig. 2.20(g)). The reconstructed IR pulses (not shown) have a temporal duration of 12 fs for the experiment with HH19 while for the one with HH27 the IR time duration is of 15 fs; this results are in perfect accord with the measurements done with an external FROG, that gives 13 fs for both the cases. About the XUV pulse duration we obtained around 7 fs, in case the time-delay compensated monochromator is properly align. Repeating these experiments with different random guesses, we obtain for the XUV pulse a duration of 9 ± 0.5 fs in case of HH19 and of 5 ± 0.5 fs for HH27 as it is possible to notice in figure (2.20(d)-(h)). These results are, at this moment, the shortest XUV femtosecond pulses ever measured at the output of a TDCM.

Chapter 3

Ultrafast molecular dynamics

3.1 Introduction

From quantum mechanics, it is known that a lot of dynamics that occur in atoms and molecules have temporal duration in the order of few-femtosecond, and in order to be able to investigate them ultrashort pulses are necessary. Such pulses have been generated and characterized with the setup and techniques described in the former chapters, so actually, we are able to start studying different kind of dynamics. In this chapter, first I will describe the characteristics of the molecules we are investigating, then the process of data acquisition will be presented, and, at least, the measurement results that we achieved.

3.2 Relaxation dynamics of ethylene cation

Relaxation dynamics are triggered by a few-femtosecond optical excitation pulse and define the photochemistry of many molecular systems [34], [35]. Following these ultrafast dynamics in real time is a challenging task both for theoretical and experimental physics, indeed, most of them are nowadays still unexplored despite their importance. In this scenario our attention was gained by a prototype organic molecule like ethylene, where the exact relaxation dynamics of its cation

$C_2H_4^+$ (the simplest π radical system) are not completely understood. Our setup is particular recommended for the investigation of such molecule, indeed ethylene relaxation cation can be interviewed in a pump-probe experiment. In this kind of experiment, an IR pulse induces molecular fragmentation:

$$C_2H_4^+ \longrightarrow C_2H_2^+ + H_2 \qquad 2.62\ eV \tag{3.1}$$

$$C_2H_4^+ \longrightarrow C_2H_3^+ + H \qquad 2.70\ eV \tag{3.2}$$

where the energies in eV represent the thresholds for H and H_2 elimination from the ground state [36].

A specific analysis of the temporal evolution of ions yields allow us to determine the path followed by the molecule after the excitation, and obtain interesting informations about the internal degree of freedom and conical intersections (CIs) that manage the ultrafast population transfer between cationic states, indeed transitions through CIs are responsible for the photochemistry of biomolecules [37] [38] [34] and for photostability and ultraviolet (UV) resistance of DNA [39]. At the moment, two kind of CIs have been identified to be responsible for the ultrafast relaxations dynamics, one is related to planar geometry the other is related to twisted geometry [13]. In particular, the CI associated to the planar geometry are linked with a bridged structure that should facilitate H migration preceding the loss of H_2, while the CI associated to the twisted geometry are supposed to lead the excitation of torsional vibrations [10].

In our measurement we used the 9^{th}, the 11^{th} and the 13^{th} harmonics to selectively populate the first four excited states of $C_2H_4^+$: $\tilde{X}$, $\tilde{A}$, $\tilde{B}$ and $\tilde{C}$ as shown in figure (3.1).

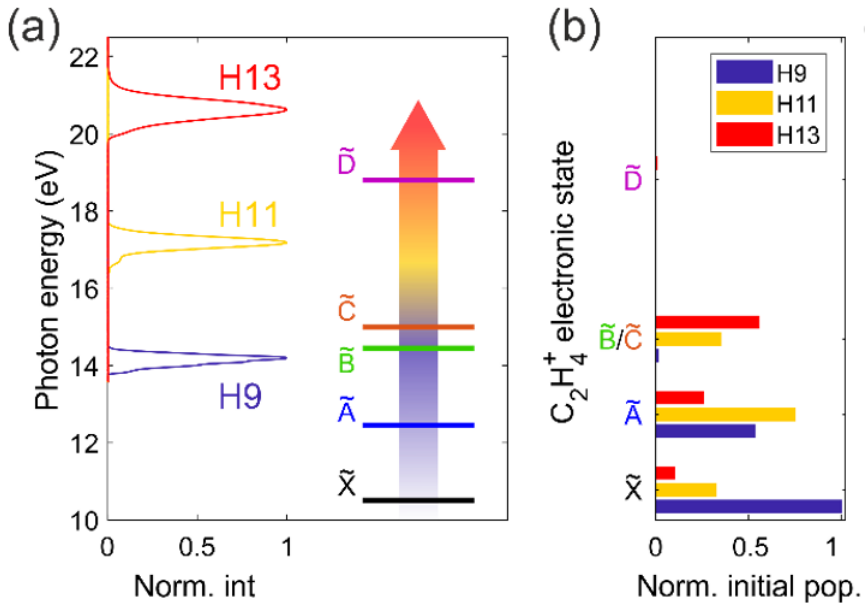

Figure 3.1: (a) XUV spectrum of the HHs used in the experiment together with the first five states of molecular cation [8]. (b) Initial state population calculated with the partial cross-section taken from [9] and harmonic spectra in (a).

In particular, it is possible to notice that H9 enables a very efficient excitation of the $\tilde{X}$ state, H11 of $\tilde{A}$ state, while H13 mainly excite $\tilde{B}$ and $\tilde{C}$ states. We estimated the time duration of each harmonic from a cross-correlation photoelectron experiment. We found that the time duration of the harmonic radiation ranges from 12 fs with H9 to 7 fs with H13.

The internal relaxation process that follows photoexcitation can eventually lead to dissociation.

The ionization of ethylene launches molecular dynamics on different cationic states that can be represented by wave packets evolving on the Potential Energy Surfaces (PES) toward the stable cation ground state or toward dissociative channels as shown in figure (3.2).

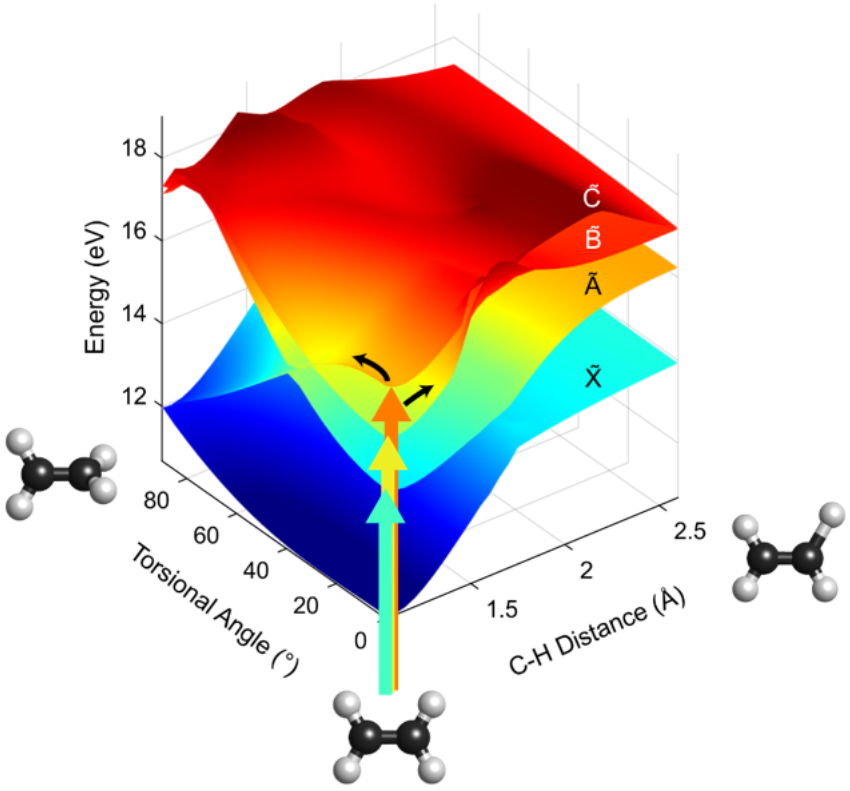

Figure 3.2: Potential Energy Surfaces (PES) for ethylene cation. In particular $\tilde{X}$ represent the ground state, while $\tilde{A}$, $\tilde{B}$ and $\tilde{C}$ represent the first three exited states (adapted from [10]).

After the initial XUV ionization and excitation, the electronic charge will redistribute and initiate the molecular motion through which the molecules relaxes as shown in figure (3.3.a). If an IR pulse arrives while the relaxation is occurring, it could introduce an additional fragmentation with a loss of one or two hydrogen atoms (3.3.b).

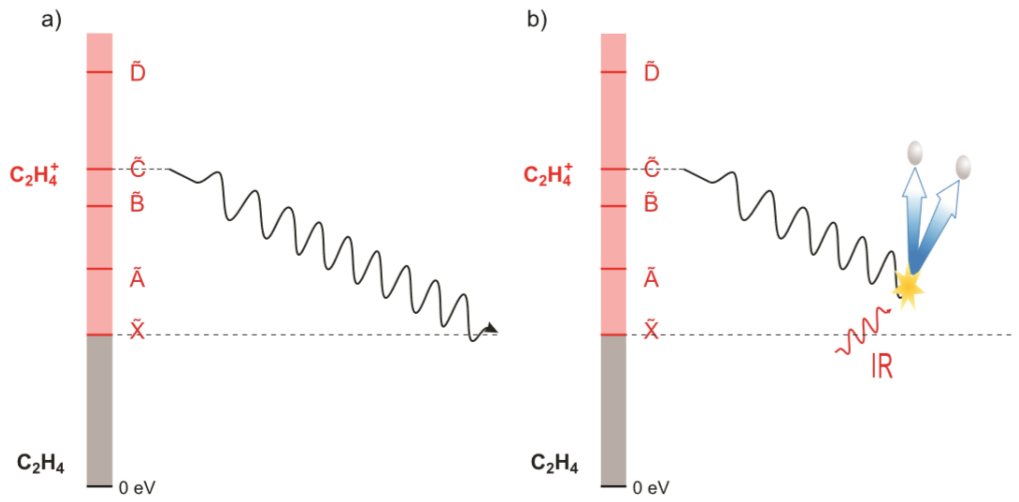

Figure 3.3: (a) Schematic representation of the internal relaxation from an excited cation state to its ground state after XUV excitation. (b) After a certain delay (properly defined) the IR pulse can stop the relaxation process by giving the molecule sufficient energy to lose one of two H atoms (adapted from [11]).

Interrupting the relaxation process is important in order to understand the molecular properties of ethylene, in particular the temporal characteristics of the dynamics: after C_2H_4 has been excited, it begins to relax to the ground state, but if we interrupt this relaxation process with an IR pulse, fragmentation will happen and there will be a reduction of $C_2H_4^+$ and an increase of the ions $C_2H_2^+$ and $C_2H_3^+$.

The energy of XUV photons is also related to the fragmentation process, indeed different harmonics produce different ions as shown in figure (3.4). Selecting one specific harmonic allows to generate specific ions, and this property will be considered in our experiments with different harmonics

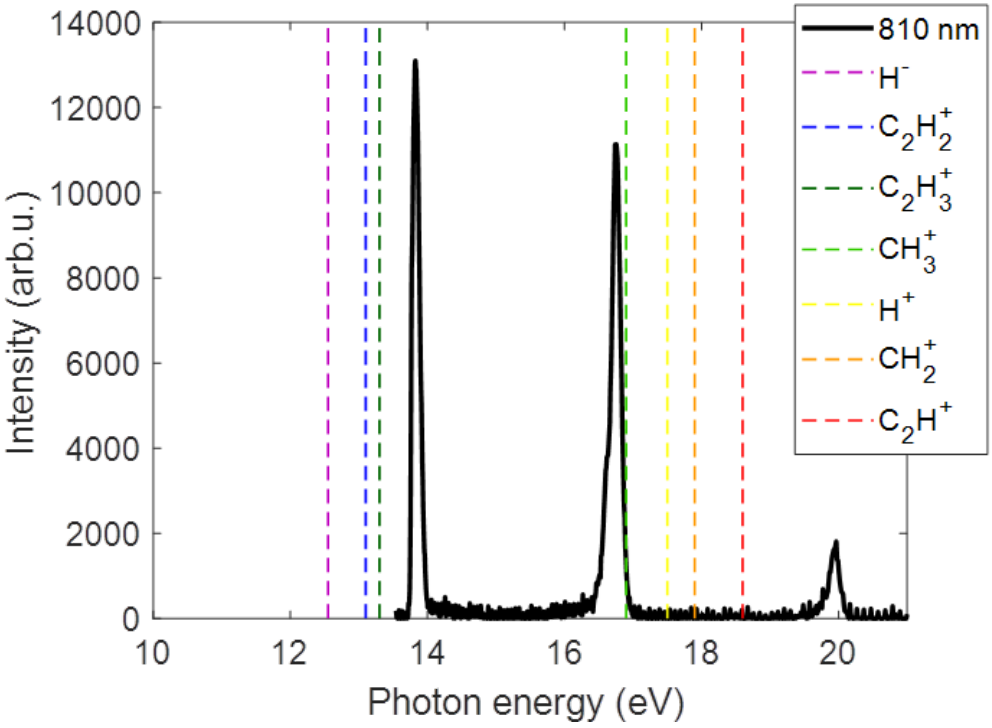

Figure 3.4: Harmonic spectrum in an energetic scale. From left to right there are shown H9 ($\approx$ 14 eV), H11 ($\approx$ 17 eV) and H13 ($\approx$ 20 eV), and in dotted line the fragmentation threshold energy.

3.3 Measurement process

The acquisition process is based on the use of a time-of-flight (TOF) spectrometer. First of all, ethylene is injected inside the TOF with a needle. The gas pressure reached is around $6 \cdot 10^{-6}$ $mbar$ after a period of stabilization of around one hour. Then the TOF is set in electrons mode, so that a scan (where XUV generates photoelectrons and changing the delay between the harmonic and the IR pulses we can see the sidebands) is taken in order to find two significant data: the delay value at which temporal superposition between the XUV and IR pulses is maximum, and the sideband time duration. Then an ion measurement is done: the XUV pulse at a specific harmonic interacts with the ethylene molecules and induces ionization, so, applying a voltage difference, ions are collected. They fly along a drift tube that accelerates them, and they are focused thanks an

electrostatic lens. They are detected thanks a Multi-Channel Plate (MCP) that generates a properly amplified signal in correspondence of the ion detected. The time of flight of each ion is directly proportional to the mass of the ion itself:

$$t(m) = \sqrt{\frac{m}{2Vq}}\, L \tag{3.3}$$

where L is the length of the drift tube, V is the potential difference felt by ions and q is the ions charge. So, the equation (3.3) shows that knowing the time of flight of each ions it is possible to retrieve the masses of all the ions detected.

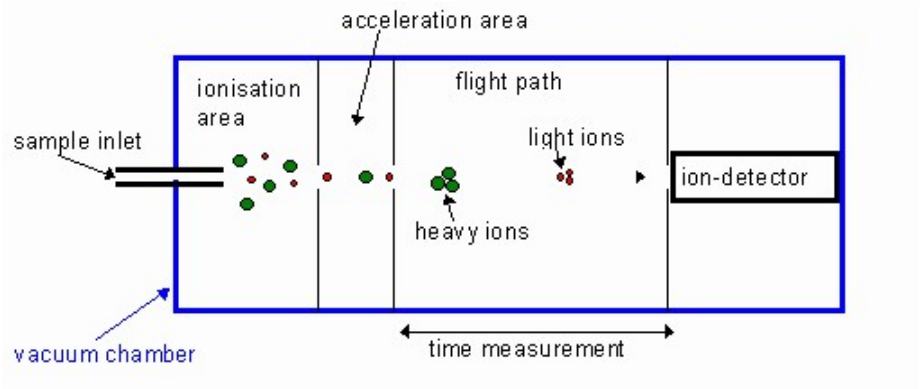

Figure 3.5: Schematic representation of a time of flight spectrometer (TOF). TOF can work both in electron and ion mode, in particular in the image ion mode is activated: the sample is injected inside the spectrometer thanks to a needle, then the laser pulse ionize the gas so that ions can be extracted, so that they are free to move along the drift tube and they can be detected by a MCP.

The signal in output from the ion detector is sampled by the data acquisition (DAQ) of an oscilloscope that for each delay mediates on 4000 acquisitions. Anyway, the signal from the MCP is not sufficient to determine the mass of the ions, because the acquisition must be triggered by en external signal. The trigger that we used is obtained by a photodiode placed in the proximity of one of the chirped mirrors after the hollow core fiber, such that a loss of the signal indicates that the pulse is passed. When the oscilloscope receives the trigger pulse it starts sampling the incoming ions. A complete scan is done changing the delay between the XUV pulse and IR, sampling delay per delay, so that, a

spectrogram is obtained. On the x axis is present the delay between the XUV and IR pulses, while on y axis there is the mass of those ions detected. In order to evaluate the ion yield, a measure is taken with the IR pulse, and the other without the IR; this measurement is taken with the aid of an electrical shutter driven by the LabVIEW VI that manages the entire scan. In such a way we are able to determine the how much the measurement is effected by the IR. This process is repeated four times for each scan in order to have enough statistics and improve the quality of the measurement considering a mediation.

After the acquisition process, we analyzed the obtained data. In order to correctly interpret the results, first of all, a mass calibration is required, so that it is possible to identify all the ions detected by the sensor; then, for a given ion of atomic mass X $a.m.u.$ we construct the total yield signal integrating the output current from the TOF, considering an integration window centered on the X $a.m.u.$ value and large 0.25 $a.m.u.$ for each side, so that it goes from $X - 0.25$ $a.m.u.$ to $X + 0.25$ $a.m.u.$. This signal is a representation of how the presence of the particular ion is modified by the delay variation between the XUV and IR pulses. The ion yield is then achieved by the subtraction of the measure taken with IR pulse and the one without the IR:

$$Y = Y_{ON} - Y_{OFF} \tag{3.4}$$

This signal is then fitted with a curve given by two main terms, one growing that represents the ions decay, the other that describes a formation:

- **Decay**

$$g(t) = \frac{1}{\sigma\sqrt{2\pi}} e^{-\frac{(\mu-t)^2}{2\sigma^2}} \tag{3.5}$$

$$f(t) = \alpha e^{-\alpha t} H(t) \tag{3.6}$$

$$EMG(t) = g(t) * f(t) = \frac{\alpha}{2} e^{\frac{\alpha}{2}(2\mu+\alpha\sigma^2-2t)} erfc\left(\frac{\mu+\alpha\sigma^2-t}{\sqrt{2}\sigma}\right) \tag{3.7}$$

- **Formation**

$$g(t) = \frac{1}{\sigma\sqrt{2\pi}} e^{-\frac{(\mu-t)^2}{2\sigma^2}} \tag{3.8}$$

$$f'(t) = \alpha(1 - e^{-\alpha t})H(t) \tag{3.9}$$

$$\begin{aligned} EMG'(t) &= g(t) * f'(t) \\ &= \frac{\alpha}{2}\left[erfc\left(\frac{\mu - t}{\sqrt{2}\sigma}\right) - e^{\frac{\alpha}{2}(2\mu+\alpha\sigma^2-2t)} erfc\left(\frac{\mu + \alpha\sigma^2 - t}{\sqrt{2}\sigma}\right)\right] \end{aligned} \tag{3.10}$$

where $g(t)$ is the response of the system, represented by a Gaussian function centered on the mean value μ with a standard deviation σ, $f(t)$ is an exponential term with α describing a proper amplitude multiplied by the Heaviside function, and, EMG is the Exponential Modified Gaussian that is the convolution of the exponential term times the Gaussian.

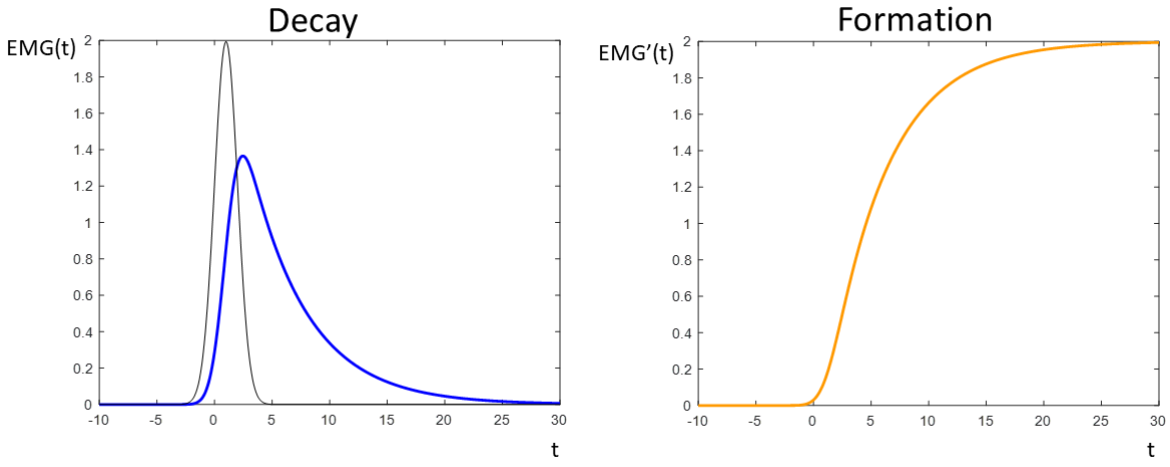

Figure 3.6: Graphics of the equations describing the decay and formations terms.

In the next section will be presented the obtained results.

3.4 Experimental results

In figure 3.1(c) are shown the main fragments produced by photoexcitation with the XUV pulses. As a consequence of selective excitation, the fragment yields pertaining to different harmonics qualitatively differ from each other. In order to study the ultrafast relaxation dynamics of $C_2H_4^+$, in our measurements, XUV has been used as pump, then IR has been used as probe.

The temporal evolution of the ion yield has been detected as function of the relative delay between the two pulses. It is important to consider that the interaction of the molecular ion with the IR pulses can determine significant modifications to the relaxation process, deviating the molecule from its natural relaxation path, so that a change in the fragmentation process is obtained. Consequently, the transient features in the relative delay-dependent ion yields contain a fingerprint of the ultrafast molecular dynamics.

In our this experiments the IR was set at an intensity of 16 mW.

3.4.1 Harmonic 9

As shown in figure (3.1), harmonic 9 initially populates prevalently the $\tilde{X}$ state and in a minor way also the $\tilde{A}$ state. As one can already guess from the fragmentation threshold energy (figure 3.4), the main dynamics are observed for the ions $C_2H_2^+$, $C_2H_3^+$ and $C_2H_4^+$. In the following I report the ions yields which present a clear IR-induced dynamic:

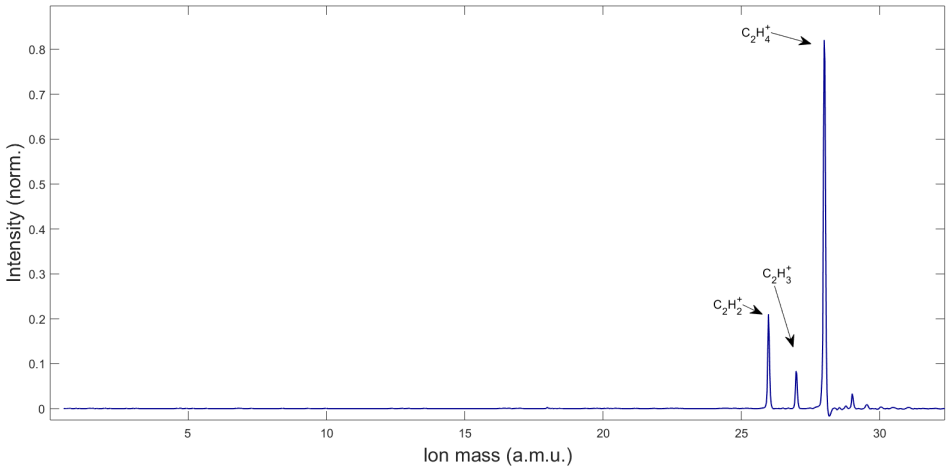

Figure 3.7: Ion mass spectrum from harmonic 9.The arrows mark $C_2H_2^+$, $C_2H_3^+$, $C_2H_4^+$.

Cation $C_2H_2^+$

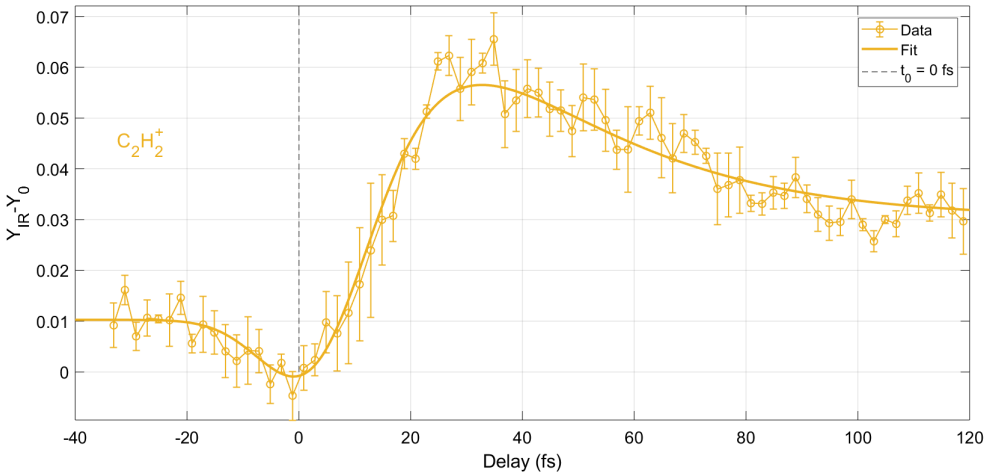

Figure 3.8: $C_2H_2^+$ yield as function of the delay between the two pulses, in the case of H9. Experimental data and a proper fitting are shown with a value t_0 that represents the point at which the dynamics begins.

For this ion yield, represented in figure (3.8) we considered a fitting composed by one decay term and one formation term, described by equations (3.7) and (3.10). We considered both the terms because, assuming just a decay the fitted curve had a cross-correlation much longer than the one measured with the electrons, but considering also a formation term, the cross-correlation values were quite similar. In this case the decay time constant is $\tau_{decay} = 11.6\ fs$ while

the formation time constant is $\tau_{formation} = 25.5\ fs$. The dynamics is supposed to begin at $t_0 = 0\ fs$ and the measured cross-correlation is 19.5 fs that is really close to the one measured with electrons $18.9 \pm 2.3\ fs$.

Cation $C_2H_3^+$

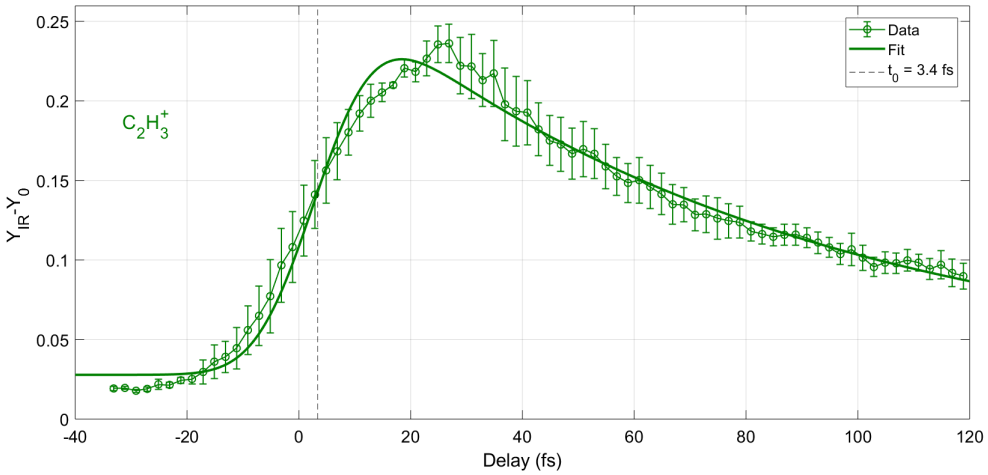

Figure 3.9: $C_2H_3^+$ yield as function of the delay between the two pulses, in the case of H9. Experimental data and a proper fitting are shown with a value t_0 that represents the point at which the dynamics begins.

In this case, displayed in figure (3.9), we just used a decay term for the fit equation, indeed, no formation seems to occur. In particular, the decay time constant is $\tau_{decay} = 80.3\ fs$ that indicates a longer dynamics respect the one in figure (3.8). The dynamics is supposed to begin at $t_0 = 3.4\ fs$ and the measured cross-correlation is 20.1 fs while the one given from electrons measurement is $18.9 \pm 2.3\ fs$.

cation $C_2H_4^+$

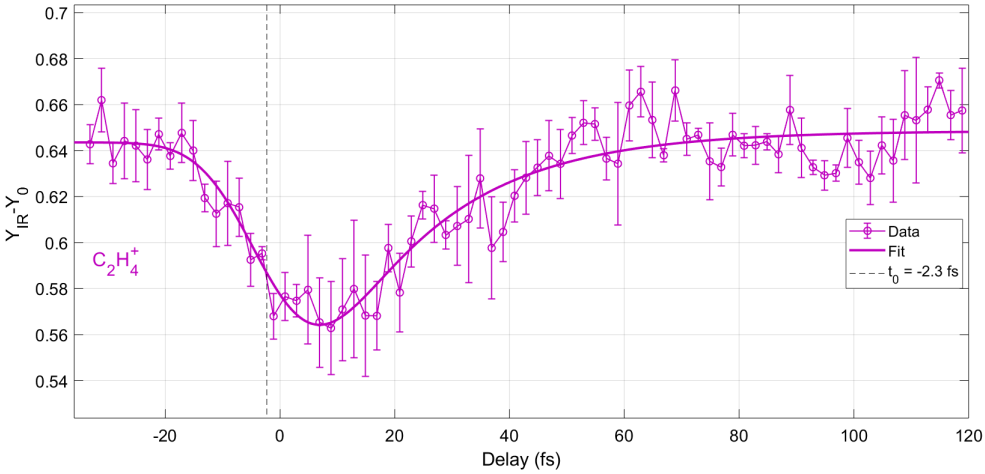

Figure 3.10: $C_2H_4^+$ yield as function of the delay between the two pulses, in the case of H9. Experimental data and a proper fitting are shown with a value t_0 that represents the point at which the dynamics begins.

Also in this case, represented in figure (3.10), a decay component is sufficient for the fitting curve. In particular the decay time constant is $\tau_{decay} = 20.6\ fs$ and the begin of the dynamics is supposed to be at $t_0 = -2.3\ fs$; in order to explain this negative value it is necessary to consider the errorbar given by the curve fit, indeed t_0 is just the center of a confidence interval at 95%: $[-2.3 \pm 6.2\ fs]$. Considering the measured cross-correlation to be 19.9 fs while the one given from electrons measurement is $18.9 \pm 2.3\ fs$.

3.4.2 Harmonic 11

Harmonics 11 is able to excite essentially state $\tilde{A}$. Referring to figure (3.4) this harmonic causes mainly fragmentation of $C_2H_2^+$, $C_2H_3^+$ and $C_2H_4^+$, but when the XUV and IR pulses are temporal overlapped the IR gives sufficient additional energy to the molecule to produce CH_2^+ and H^+ upon fragmentation. For this reason these latter ions show a clear and strong pump dependence.

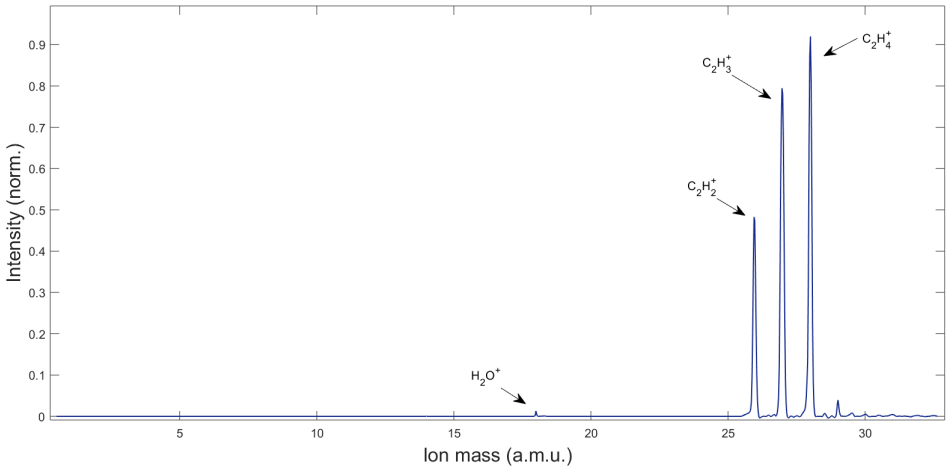

Figure 3.11: Ion mass spectrum from harmonic 11. In particular there are $C_2H_2^+$, $C_2H_3^+$, $C_2H_4^+$. This spectrum has been considered at the beginning of the scan, so others ions are not still visible. H_2O^+ comes from the background

Cation $C_2H_2^+$

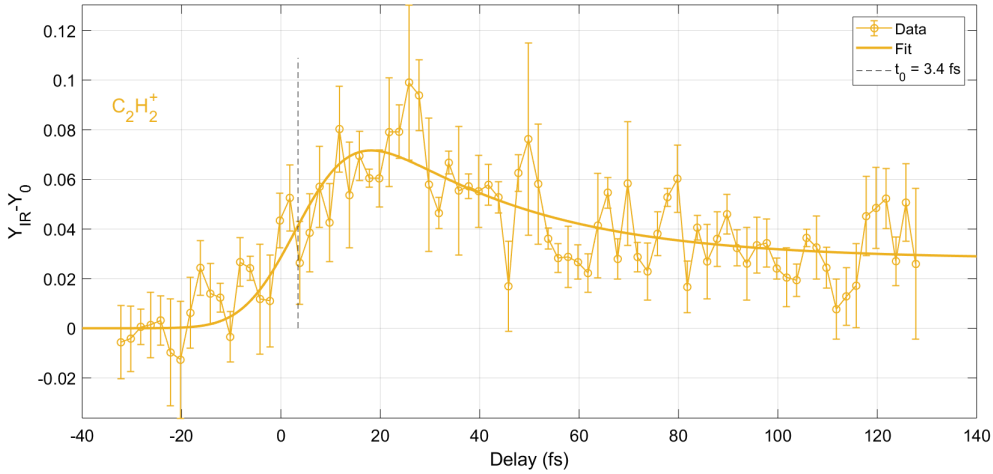

Figure 3.12: $C_2H_2^+$ yield as function of the delay between the two pulses, in the case of H11. Experimental data and a proper fitting are shown with a value t_0 that represents the point at which the dynamics begins.

For this ion, displayed in figure (3.12), we noticed that applying just a decay term for the fitting curve we obtained a cross-correlation value very different respect the one measured with the electrons scan that is $19.9 \pm 3.3\ fs$. For this reason we adopted both a decay and a formation term, obtaining a cross-correlation of 20.1 fs. The decay time constant is $\tau_{decay} = 31.2\ fs$, while the

formation time constant is $\tau_{formation} = 7.6\ fs$. The begin of the dynamics is supposed to be at $t_0 = 3.4\ fs$.

Cation $C_2H_3^+$

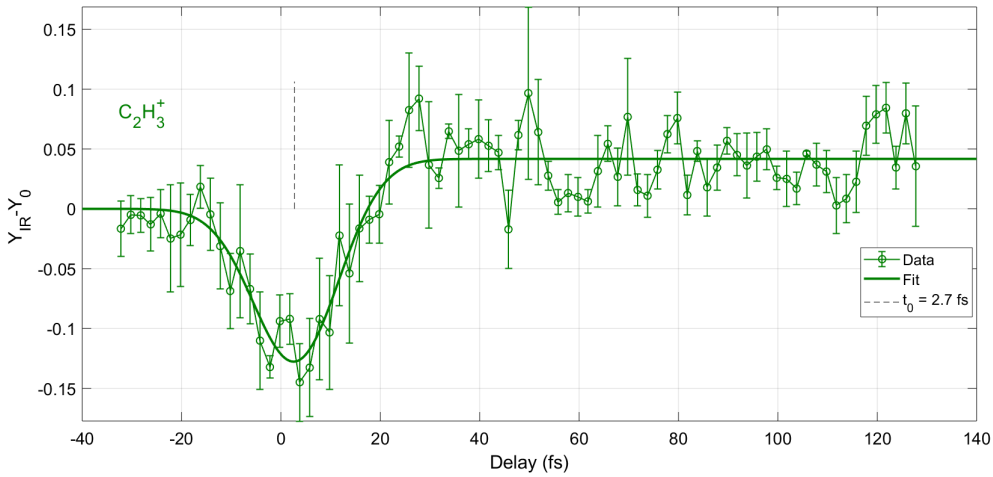

Figure 3.13: $C_2H_3^+$ yield as function of the delay between the two pulses, in the case of H11. Experimental data and a proper fitting are shown with a value t_0 that represents the point at which the dynamics begins.

Also in this case, figure (3.13), we used a decay term plus a formation term. The temporal constant for decay is $\tau_{decay} = 0.8\ fs$, and for the formation is $\tau_{formation} = 0.8\ fs$. This could means that the dynamics is really fast. The dynamics starts at $t_0 = 2.7\ fs$ and the temporal duration of the measured cross-correlation is $20.2\ fs$ while the one given by the electrons scan is $19.9 \pm 3.3\ fs$.

Cation $C_2H_4^+$

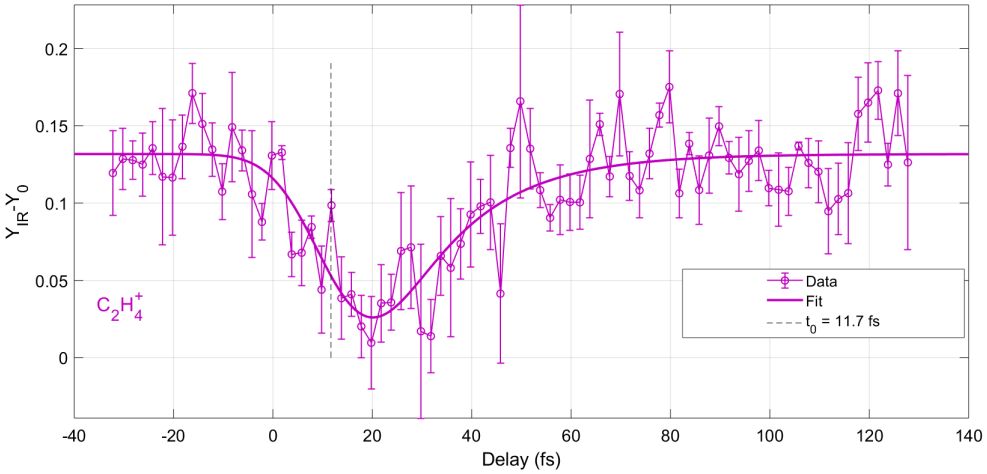

Figure 3.14: $C_2H_4^+$ yield as function of the delay between the two pulses, in the case of H11. Experimental data and a proper fitting are shown with a value t_0 that represents the point at which the dynamics begins.

In figure (3.14) no formation seems to be present, so for this fitting curve we just use a decay term, with a temporal constant $\tau_{decay} = 16.1\ fs$. The dynamics starts at $t_0 = 11.7\ fs$ and the temporal duration of the measured cross-correlation is 20.2 fs that is really close to the one given by the electrons scan $19.9 \pm 3.3\ fs$.

Cation CH_2

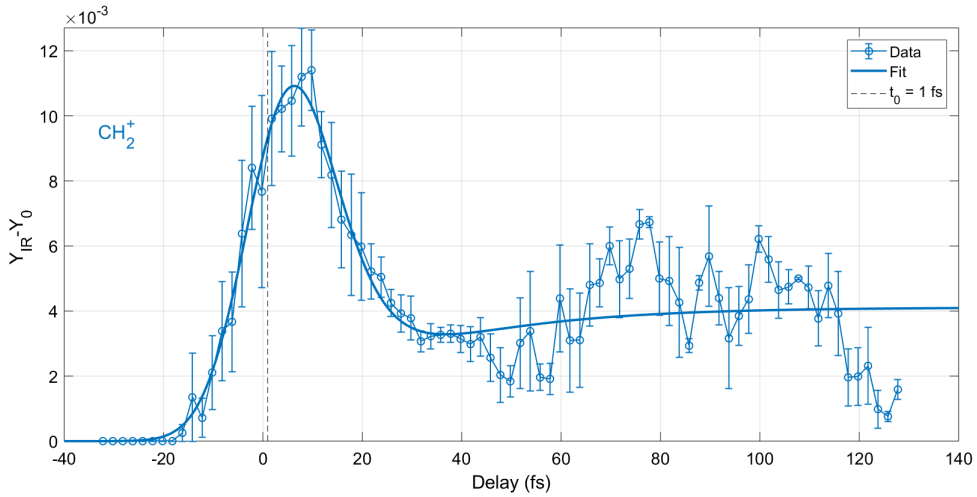

Figure 3.15: CH_2^+ yield as function of the delay between the two pulses, in the case of H11. Experimental data and a proper fitting are shown with a value t_0 that represents the point at which the dynamics begins.

This ion, which yield is shown in figure (3.15), is not present until the IR pulse is not overlapped with the XUV. The reason of this phenomenon is that H11 alone is not sufficiently energetic to induce the fragmentation of CH_2 as shown in figure (3.4), but with the IR pulse, the energy gap is filled and this ion can be generated. For the fitting we used both the components. The temporal constant of the decay term is $\tau_{decay} = 5.9\ fs$ and the formation time constant is $\tau_{formation} = 25.7\ fs$. The dynamics starts at $t_0 = 1\ fs$ and the temporal duration of the cross-correlation is 19.2 fs quite close to the one measured from electrons scan $19.9 \pm 3.3\ fs$.

Cation H^+

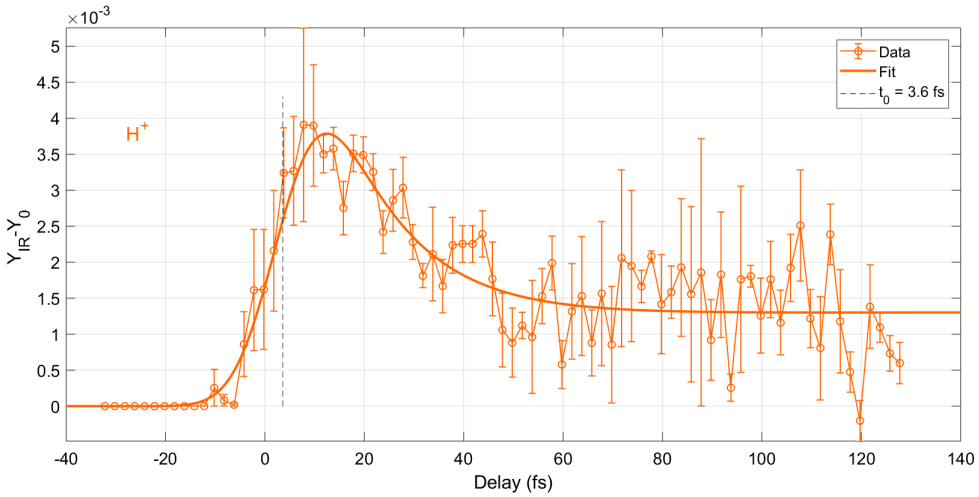

Figure 3.16: H^+ yield as function of the delay between the two pulses, in the case of H11. Experimental data and a proper fitting are shown with a value t_0 that represents the point at which the dynamics begins.

As in the case of CH_2, this ion is not generated until the superposition of XUV and IR pulses is reached. For the fitting curve we considered the sum of the decay equation plus the formation equation with the temporal constant $\tau_{decay} = 16.3\ fs$ and $\tau_{formation} = 23\ fs$. The dynamics starts at $t_0 = 3.6\ fs$ and the temporal duration of the cross-correlation is 16.8 fs while the one given by the electron scan is $19.9 \pm 3.3\ fs$.

3.4.3 Harmonic 13

Harmonic 13 is the most energetic harmonic that we used in our experiments. It is able to excite mainly the states $\tilde{B}$ and $\tilde{C}$ as shown in figure (3.1). Due its higher energy it is able to fragment $C_2H_4^+$ and generate many ions: H^+, CH_2^+, $C_2H_2^+$, $C_2H_3^+$ and $C_2H_4^+$ as displaced in figure (3.17), but not all of them present dynamics.

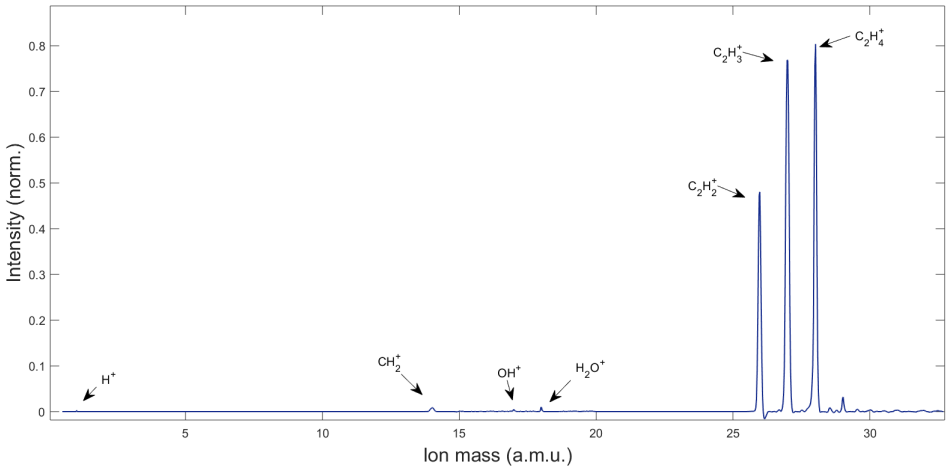

Figure 3.17: Ion mass spectrum from harmonic 13. In particular there are, from left to right, H^+, CH_2^+, $C_2H_2^+$, $C_2H_3^+$, $C_2H_4^+$. OH^+ and H_2O^+ come from the background.

Cation $C_2H_2^+$

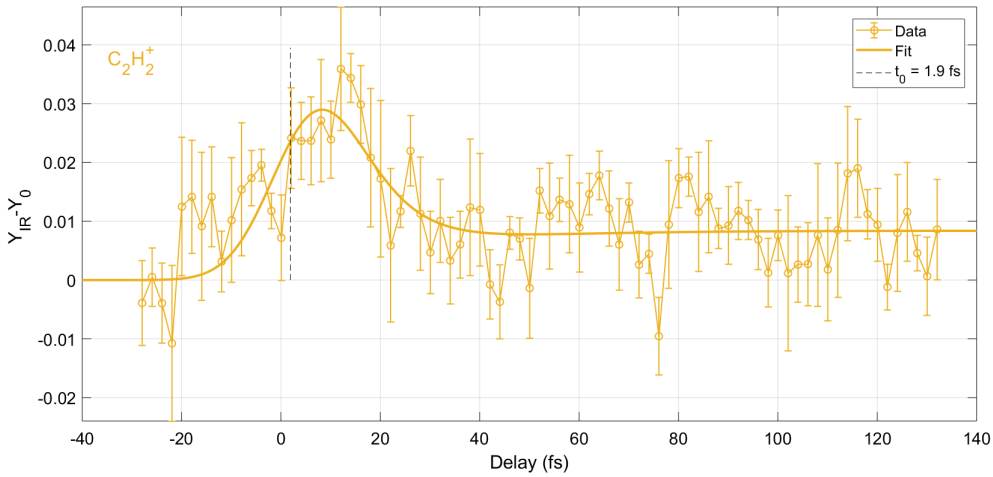

Figure 3.18: $C_2H_2^+$ yield as function of the delay between the two pulses, in the case of H13. Experimental data and a proper fitting are shown with a value t_0 that represents the point at which the dynamics begins.

In figure (3.18) it is possible to observe that his ion present a decay and a formation term. Indeed, with just one decay the cross-correlation measured was too different from the one given by the electrons scan, consequently we decided to insert also a formation term. In particular, the cross-correlation with both the terms is 19.4 fs and the temporal duration of the one given by the electrons

scan is $17.5 \pm 3.8\ fs$. The time constant of the decay is $\tau_{decay} = 8\ fs$, while the formation time constant is $\tau_{formation} = 21.8\ fs$. The dynamics begins at $t_0 = 1.9\ fs$.

Cation $C_2H_3^+$

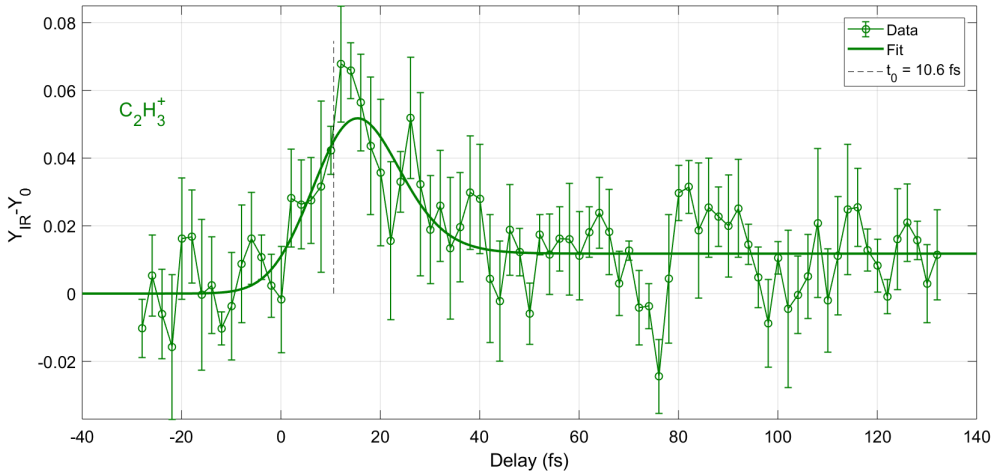

Figure 3.19: $C_2H_3^+$ yield as function of the delay between the two pulses, in the case of H13. Experimental data and a proper fitting are shown with a value t_0 that represents the point at which the dynamics begins.

As shown in figure (3.19), the fitting curve for $C_2H_3^+$ yield is composed by a decay term and a formation term. The time constant of the decay term is $\tau_{decay} = 4.7\ fs$ while the formation time constant is $\tau_{formation} = 3.1\ fs$. The dynamics begins at $t_0 = 10.6\ fs$ and the temporal duration of the cross-correlation is $18.6\ fs$ quite similar to $17.5 \pm 3.8\ fs$ obtained from the electron scan.

Cation $C_2H_4^+$

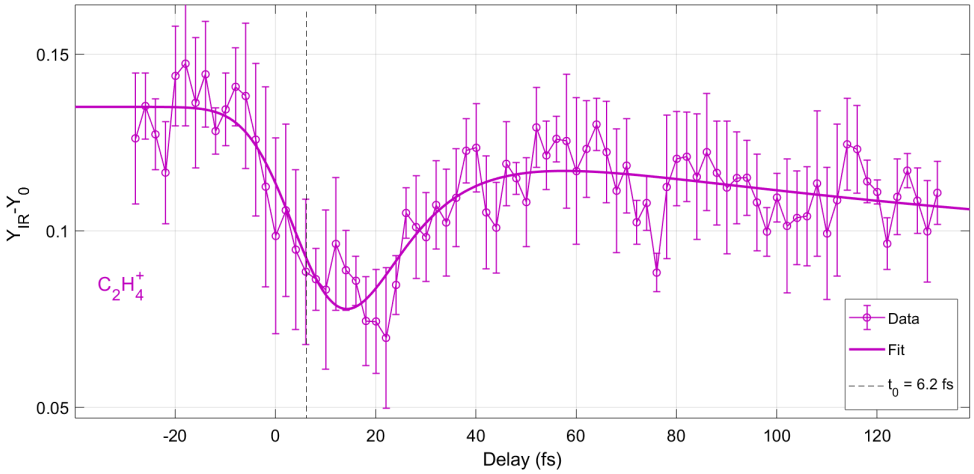

Figure 3.20: $C_2H_4^+$ yield as function of the delay between the two pulses, in the case of H13. Experimental data and a proper fitting are shown with a value t_0 that represents the point at which the dynamic begins.

In this case, as shown in figure (3.20), we noticed an uncommon behavior, indeed the experimental data decrease continuously, for this reason we introduced a negative formation term in addition to the decay used in case of H9 and H13. The time constant of the decay term is $\tau_{decay} = 13.1\ fs$ and the time constant of the formation term is $\tau_{formation} = 120.9\ fs$. The dynamics begins at $t_0 = 6.2\ fs$ and the temporal duration of the measured cross-correlation is 19.4 fs while the one obtained from the electron scan is $17.5 \pm 3.8\ fs$.

Cation C_2H^+

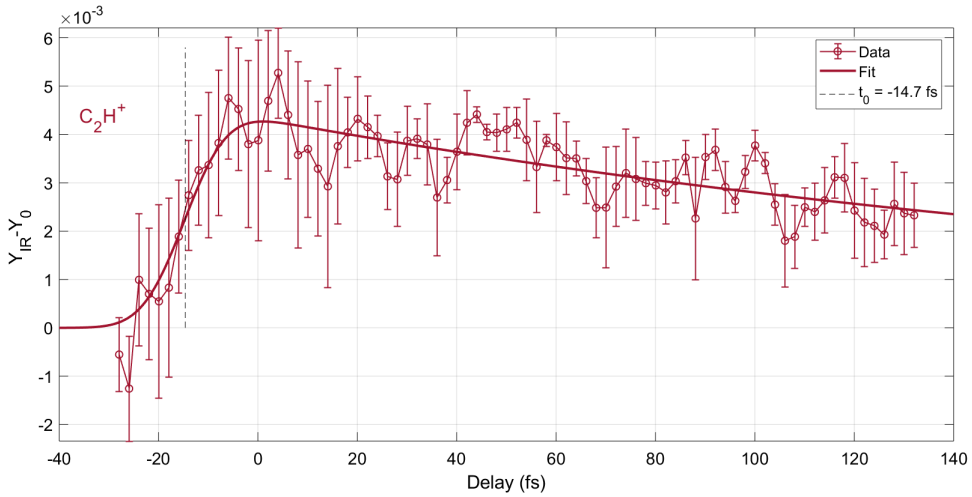

Figure 3.21: C_2H^+ yield as function of the delay between the two pulses, in the case of H13. Experimental data and a proper fitting are shown with a value t_0 that represents the point at which the dynamics begins.

In this case, as shown in figure (3.21), we assumed a fitting curve composed by a decay term, characterized by a $\tau_{decay} = 228.9\ fs$ that express a very slow dynamics. In particular, the temporal duration of the cross-correlation is 15.9 fs while the one given by the electrons scan is $17.5 \pm 3.8\ fs$.

Cation CH_2^+

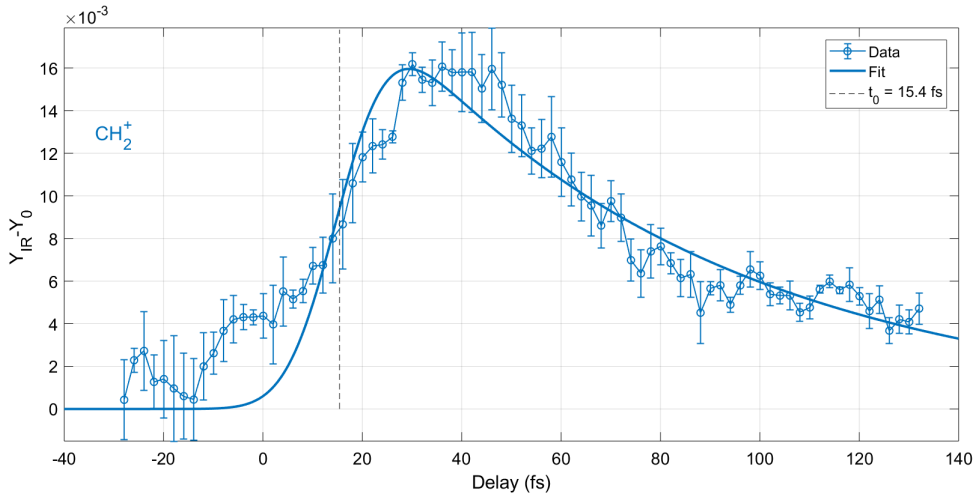

Figure 3.22: CH_2^+ yield as function of the delay between the two pulses, in the case of H13. Experimental data and a proper fitting are shown with a value t_0 that represents the point at which the dynamics begins.

For this ion, we assumed just one decay term with a temporal constant $\tau_{decay} = 67.7\ fs$. The dynamics begins at a $t_0 = 15.4\ fs$ and the temporal duration of the cross-correlation is 19.4 fs while the one given from the electrons scan is $17.5 \pm 3.8\ fs$.

Cation H^+

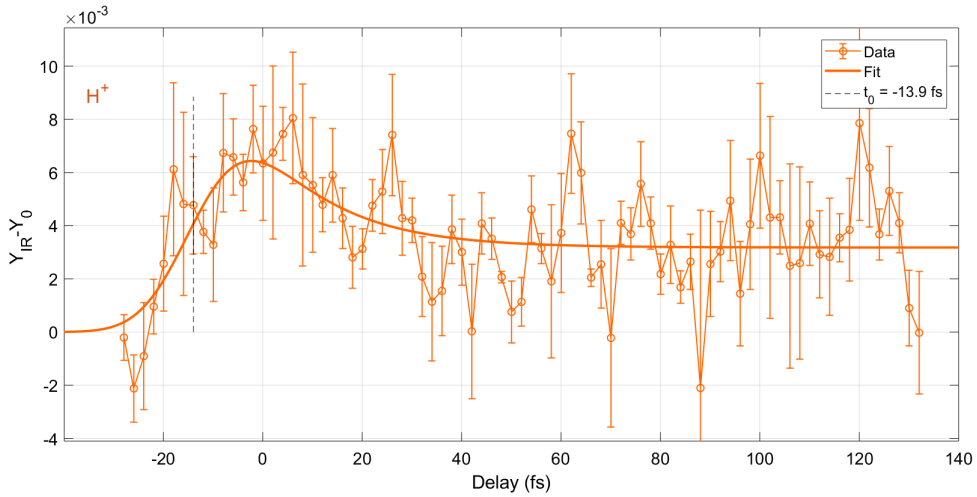

Figure 3.23: H^+ yield as function of the delay between the two pulses, in the case of H13. Experimental data and a proper fitting are shown with a value t_0 that represents the point at which the dynamics begins.

As shown in figure (3.23), H^+ ion presents a dynamics that can be fitted with a curve composed by one decay term and one formation term, with a $\tau_{decay} = 15.5\ fs$ and $\tau_{formation} = 5.1\ fs$. The temporal duration of the cross-correlation is 19.2 fs while the one given by the electron scan is $17.5 \pm 3.8\ fs$. In conclusion, from this measurement it is possible to observe that when the XUV and IR pulses are overlapped the yield signal of $C_2H_4^+$ decreases while the signal from $C_2H_2^+$ and $C_2H_3^+$ increase. We expect that the initial point of the dynamics decreases with harmonic order [13] [10], but from our measurement we are not able to confirm this model:

Table 3.1: Recap of the starting time of the dynamics for the ions $C_2H_2^+$, $C_2H_3^+$ and $C_2H_4^+$

	H9	**H11**	**H13**
$C_2H_2^+$	$0\ fs$	$3.4\ fs$	$1.9\ fs$
$C_2H_3^+$	$3.4\ fs$	$2.7\ fs$	$10.6\ fs$
$C_2H_4^+$	$-2.3\ fs$	$11.7\ fs$	$6.2\ fs$

Chapter 4

Conclusion and further development

In this thesis work we focused our attention on two main arguments. First, we developed an experimental setup that allows us to generate and characterize few-femtosecond extreme ultraviolet (XUV) pulses, then in the second part we used them to investigate ultrafast relaxation dynamics in ethylene.

After high-order harmonic generation, all the frequencies are emitted together in a pulse of a temporal duration of hundreds of attoseconds. The selection of just one harmonic is a tricky operation, that can imply the loss of the pulse temporal properties, for this reason we use a Time-Delay Compensated Monochromator (TDCM). With this approach we loose the attosecond resolution, but we gain the harmonic tunability, indeed we are able to choose odd harmonics in the range of orders: $9 \div 31$, with few-femtosecond temporal duration. The strength of our setup is then related to the possibility to choose a specific harmonic, maintaining a good temporal resolution. Having both temporal and spectral resolution is a unique property that allows us to do selective pump-probe experiments.

The challenge given by the characterization was related to the development of an algorithm to use for the reconstruction, indeed those that for attosecond

pulses give suitable results as the Principal Component Generalized Projection Algorithm (PCGPA) and the Least Squared Generalized Projection Algorithm (LSGPA), in the case of few-femtosecond they have shown to be completely inadequate, while the extended Ptychographic Iterative Engine (ePIE), properly adapted, gives good results: with this approach we reconstructed XUV pulses with the temporal duration of $5 \pm 0.5\ fs$ that, at the current moment, are the shortest ever measured.

Thanks to such pulses we were able to investigate ethylene relaxation dynamics by pump-probe experiments. The next step will be the development of suitable theoretical models, from which we expect to achieve detailed information about molecular dynamics.

The experimental setup can be greatly improved by implementing a new method for data acquisition with a faster DAQ, so that, thanks to a chopper at proper frequency, it will be possible to sample a measure with the IR on and the other with IR off, one immediately after the other, making the measurement more accurate. With this approach the measure would be quite faster and consequently less subject to any possible external instability. Another interesting way to improve the analysis of the data is to study how the IR intensity affects the results. Making measurement at different IR intensities and looking for variations of the ion yields between each intensity would allow to identify how much the IR is effecting the measurement. Harmonic tunability represent another remarkable characteristic of the experimental setup,indeed, since different fragmentation levels are near harmonic energies it is possible to investigate how ion yields change if we set the selected harmonic just below one fragmentation level or just above. The good spectral resolution of the XUV setup developed during this thesis work, in combination with few-femtosecond temporal resolution will be used to investigate ultrafast relaxation process not only in gas phase but also on solid samples.

Bibliography

[1] PB Corkum. Pb corkum, phys. rev. lett. 71, 1994 (1993). *Phys. Rev. Lett.*, 71:1994, 1993.

[2] Kenichi Ishikawa. High-harmonic generation. 02 2010.

[3] Structure of a diffraction gratings. https://www.flinnsci.com.

[4] Luca Poletto and Paolo Villoresi. Time-delay compensated monochromator in the off-plane mount for extreme-ultraviolet ultrashort pulses. *Applied optics*, 45(34):8577–8585, 2006.

[5] Matteo Lucchini, Giacinto D Lucarelli, Mario Murari, Andrea Trabattoni, Nicola Fabris, Fabio Frassetto, Sandro De Silvestri, Luca Poletto, and Mauro Nisoli. Few-femtosecond extreme-ultraviolet pulses fully reconstructed by a ptychographic technique. *Optics Express*, 26(6):6771–6784, 2018.

[6] Tae Moon Jeong and Jongmin Lee. Generation of high-intensity laser pulses and their applications. In Richard Viskup, editor, *High Energy and Short Pulse Lasers*, chapter 01. InTech, Rijeka, 2016.

[7] Structure of a chirped mirror. https://www.opticsbalzers.com.

[8] RA Mackie, SWJ Scully, AM Sands, R Browning, KF Dunn, and CJ Latimer. A photoionization mass spectrometric study of acetylene and ethylene in the vuv spectral region. *International Journal of Mass Spectrometry*, 223:67–79, 2003.

[9] Joseph Berkowitz. *Atomic and Molecular Photoabsorption: Absolute Partial Cross Sections*. Academic Press, 2015.

[10] André Ludwig, Elisa Liberatore, Jens Herrmann, Lamia Kasmi, Pablo López-Tarifa, Lukas Gallmann, Ursula Rothlisberger, Ursula Keller, and Matteo Lucchini. Ultrafast relaxation dynamics of the ethylene cation c2h4+. *The Journal of Physical Chemistry Letters*, 7(10):1901–1906, 2016.

[11] Hans Jakob Wörner, Christopher A Arrell, Natalie Banerji, Andrea Cannizzo, Majed Chergui, Akshaya K Das, Peter Hamm, Ursula Keller, Peter M Kraus, Elisa Liberatore, et al. Charge migration and charge transfer in molecular systems. *Structural Dynamics*, 4(6):061508, 2017.

[12] Yann Mairesse and F Quéré. Frequency-resolved optical gating for complete reconstruction of attosecond bursts. *Physical Review A*, 71(1):011401, 2005.

[13] Baptiste Joalland, Toshifumi Mori, Todd J Martínez, and Arthur G Suits. Photochemical dynamics of ethylene cation c2h4+. *The journal of physical chemistry letters*, 5(8):1467–1471, 2014.

[14] M. Lewenstein, Ph. Balcou, M. Yu. Ivanov, Anne L'Huillier, and P. B. Corkum. Theory of high-harmonic generation by low-frequency laser fields. *Phys. Rev. A*, 49:2117–2132, 1994.

[15] MV Ammosov, Nikolai B Delone, and Vladimir P Krainov. Tunnel ionization of complex atoms and atomic ions in a varying electromagnetic-field. *Zhurnal Eksperimentalnoi I Teoreticheskoi Fiziki*, 91(6):2008–2013, 1986.

[16] Y Mairesse, A De Bohan, LJ Frasinski, H Merdji, LC Dinu, P Monchicourt, P Breger, M Kovačev, R Taïeb, B Carré, et al. Attosecond synchronization of high-harmonic soft x-rays. *Science*, 302(5650):1540–1543, 2003.

[17] G Sansone, E Benedetti, J-P Caumes, S Stagira, C Vozzi, S De Silvestri, and M Nisoli. Control of long electron quantum paths in high-order harmonic generation by phase-stabilized light pulses. *Physical Review A*, 73(5):053408, 2006.

[18] M Lewenstein, J Mostowski, and M Trippenbach. Multichannel decay and continuum-continuum transitions in above-threshold ionisation. *Journal of Physics B: Atomic and Molecular Physics*, 18(14):L461, 1985.

[19] M Yu Ivanov and K Rzążewski. Are free-free transitions a good basis for nonlinear optics? *Journal of Modern Optics*, 39(12):2377–2381, 1992.

[20] Nikolaj B Delone and Vladimir Pavlovich Kraĭnov. *Atoms in strong light fields*, volume 28. Springer-Verlag, 1985.

[21] Dong Gun Lee, Hyun Joon Shin, Yong Ho Cha, Kyung Han Hong, Jung-Hoon Kim, and Chang Hee Nam. Selection of high-order harmonics from a single quantum path for the generation of an attosecond pulse train. *Physical Review A*, 63(2):021801, 2001.

[22] Philippe Balcou, Pascal Salieres, Anne L'Huillier, and Maciej Lewenstein. Generalized phase-matching conditions for high harmonics: The role of field-gradient forces. *Physical Review A*, 55(4):3204, 1997.

[23] Katalin Varjú‖, Yann Mairesse, B Carré, Mette B Gaarde, Per Johnsson, S Kazamias, Rodrigo López-Martens, Johan Mauritsson, KJ Schafer, Ph Balcou, et al. Frequency chirp of harmonic and attosecond pulses. *Journal of Modern Optics*, 52(2-3):379–394, 2005.

[24] Webster Cash. Echelle spectrographs at grazing incidence. *Applied optics*, 21(4):710–717, 1982.

[25] Mazyar Sabbar, Sebastian Heuser, Robert Boge, Matteo Lucchini, Thomas Carette, Eva Lindroth, Lukas Gallmann, Claudio Cirelli, and Ursula Keller. Resonance effects in photoemission time delays. *Physical review letters*, 115(13):133001, 2015.

[26] Luca Poletto, Paolo Villoresi, Enrico Benedetti, Federico Ferrari, Salvatore Stagira, Giuseppe Sansone, and Mauro Nisoli. Intense femtosecond extreme ultraviolet pulses by using a time-delay-compensated monochromator: erratum. *Optics Letters*, 33(2):140–140, 2008.

[27] Rick Trebino, Kenneth W DeLong, David N Fittinghoff, John N Sweetser, Marco A Krumbügel, Bruce A Richman, and Daniel J Kane. Measuring ultrashort laser pulses in the time-frequency domain using frequency-resolved optical gating. *Review of Scientific Instruments*, 68(9):3277–3295, 1997.

[28] J Itatani, F Quéré, Gennady L Yudin, M Yu Ivanov, Ferenc Krausz, and Paul B Corkum. Attosecond streak camera. *Physical review letters*, 88(17):173903, 2002.

[29] Daniel J Kane. Recent progress toward real-time measurement of ultrashort laser pulses. *IEEE Journal of Quantum Electronics*, 35(4):421–431, 1999.

[30] Justin Gagnon, Eleftherios Goulielmakis, and Vladislav S Yakovlev. The accurate frog characterization of attosecond pulses from streaking measurements. *Applied Physics B*, 92(1):25–32, 2008.

[31] Michael Chini, Steve Gilbertson, Sabih D Khan, and Zenghu Chang. Characterizing ultrabroadband attosecond lasers. *Optics express*, 18(12):13006–13016, 2010.

[32] D Spangenberg, E Rohwer, Michael Heinrich Brügmann, and Thomas Feurer. Ptychographic ultrafast pulse reconstruction. *Optics letters*, 40(6):1002–1005, 2015.

[33] Matteo Lucchini, MH Brügmann, André Ludwig, Lukas Gallmann, Ursula Keller, and Thomas Feurer. Ptychographic reconstruction of attosecond pulses. *Optics express*, 23(23):29502–29513, 2015.

[34] Dario Polli, Piero Altoè, Oliver Weingart, Katelyn M Spillane, Cristian Manzoni, Daniele Brida, Gaia Tomasello, Giorgio Orlandi, Philipp Kukura, Richard A Mathies, et al. Conical intersection dynamics of the primary photoisomerization event in vision. *Nature*, 467(7314):440, 2010.

[35] MCE Galbraith, S Scheit, NV Golubev, G Reitsma, N Zhavoronkov, V Despré, F Lépine, AI Kuleff, MJJ Vrakking, O Kornilov, et al. Few-femtosecond passage of conical intersections in the benzene cation. *Nature communications*, 8(1):1018, 2017.

[36] Roger Stockbauer and Mark G Inghram. Threshold photoelectron–photoion coincidence mass spectrometric study of ethylene and ethylene-d 4. *The Journal of Chemical Physics*, 62(12):4862–4870, 1975.

[37] RW Schoenlein, LA Peteanu, RA Mathies, and CV Shank. The first step in vision: femtosecond isomerization of rhodopsin. *Science*, 254(5030):412–415, 1991.

[38] Remedios González-Luque, Marco Garavelli, Fernando Bernardi, Manuela Merchán, Michael A Robb, and Massimo Olivucci. Computational evidence in favor of a two-state, two-mode model of the retinal chromophore photoisomerization. *Proceedings of the National Academy of Sciences*, 97(17):9379–9384, 2000.

[39] Mario Barbatti, Adélia JA Aquino, Jaroslaw J Szymczak, Dana Nachtigallová, Pavel Hobza, and Hans Lischka. Relaxation mechanisms of uv-photoexcited dna and rna nucleobases. *Proceedings of the National Academy of Sciences*, 107(50):21453–21458, 2010.